PHYSICAL REVIEW B **106**, 035111 (2022)

Microscopic theory of superconducting phase diagram in infinite-layer nickelates

T. Y. Xie,[1,3,*] Z. Liu,[2,3,*] Chao Cao,[1] Z. F. Wang,[2] J. L. Yang,[2] and W. Zhu[3,†]
[1]*Department of Physics, Zhejiang University, Hangzhou 310027, China*
[2]*Hefei National Laboratory for Physical Sciences at the Microscale, University of Science and Technology of China,*
Hefei, Anhui 230026, China
[3]*Key Laboratory for Quantum Materials of Zhejiang Province, School of Science, Westlake University, Hangzhou 310024, China*

(Received 9 December 2021; revised 23 June 2022; accepted 24 June 2022; published 7 July 2022)

Since the discovery of superconductivity in infinite-layer nickelates $RNiO_2$ (R = La, Pr, Nd), great research efforts have been made to unveil its underlying superconducting mechanism. However, the physical origin of the intriguing hole-doped superconductivity phase diagram, characterized by a superconductivity dome sandwiched between two weak insulators, is still unclear. Here we present a microscopic theory for the electronic structure of nickelates from a fundamental model-based perspective. We found that the appearance of weak insulator phase in lightly and heavily hole-doped regime is dominated by Mottness and Hundness, respectively, exhibiting a unique orbital-selective doping originated from the competition of Hund interaction and crystal field splitting. Moreover, the superconducting phase can also be created in the "mixed" transition regime between Mott-insulator and Hund-induced correlated state, exactly reproducing the experimentally observed superconducting phase diagram. Our findings not only demonstrate the orbital-dependent strong-correlation physics in Ni $3d$ states but also provide a unified understanding of superconducting phase diagram in hole-doped infinite-layer nickelates, which are distinct from the well-established paradigms in cuprates and iron pnictides.

DOI: 10.1103/PhysRevB.106.035111

I. INTRODUCTION

To decipher how superconductivity (SC) emerges from normal state is a crucial step towards the physical understanding of unconventional superconductor [1–8]. In early paradigms, the charge-transfer insulator [5] and bad metal [9] is used as parent compounds for cuprates [2,4] and iron pnictides [9,10], respectively. Since the exotic SC mechanism is rooted in different origins of the correlation in normal state, the exploration of new paradigm for SC is of great importance, which could further enrich the zoology of unconventional SC in strongly correlated materials. The discovery of SC in infinite-layer nickelates $RNiO_2$ (R = La, Pr, Nd) [11–19] offers a new platform for investigating the mechanism of unconventional SC. Especially, there are two key features in its experimental SC phase diagram, which are absence in cuprates and iron pnictides: (i) weak insulator in both lightly and heavily hole-doped regimes [12–16] and (ii) SC dome. sandwiched between two weak insulator regimes [12–14]. Currently, the origin of this anomalous SC phase diagram remains outstanding. It is highly desirable to explore the strong-correlation physics behind this SC phase diagram and make a possible connection to or distinction from the well-established SC mechanisms in cuprates and iron pnictides.

Although the SC mechanism in infinite-layer nickelates is a controversial topic, there have been several theoretical proposals regarding its electronic structures. The normal state is more proximate to a Mott-Hubbard insulator [20–24]. The correlation in the Ni $3d_{x^2-y^2}$ orbital is relevant to SC because of the structure analogy to cuprates [25,26]. The Ni $3d$ states are influenced by a self-doping rare-earth-orbital band (served as a charge reservoir) through a hybridization effect [27–30]. However, the appearance of itinerant electronic band cannot interpret the weakly insulating phase in heavily hole-doped regime [31–33]. Very recently, intensive studies have also demonstrated the importance of multi-Ni-orbital nature and concomitant Hund's interaction [34–51]. Nevertheless, the role of multiorbitals in the SC phase diagram is still elusive. Taken as a whole, despite various works on normal state properties, a complete and unified physical understanding of the experimental SC phase diagram on hole-doping remains unexplored.

In this work, driven by recent x-ray experimental observations [52] and first-principles calculations, we build a microscopic two-band Hubbard model with Ni $\{3d_{x^2-y^2}, 3d_{xy}\}$ orbitals. Based on mean-field calculations and interplay analysis of Hund interaction (J_H) and crystal field splitting (η), we directly identify a theoretical SC phase diagram with remarkable features: (i) weakly insulator phase dominated by orbital-selective Mottness-like physics in a lightly hole-doped regime, (ii) weakly insulator phase dominated by moderate J_H selected Hundness-like physics in a heavily hole-doped regime, and (iii) a SC phase with d-wave paring symmetry between two weakly insulators in an optimal hole-doped regime. Our results provide a microscopic model and unified physical picture for describing the electronic structures and understanding the SC phase diagram in nickelates [11–19], that

---

[*]These authors contributed equally to this work.

[†]Corresponding author: zhuwei@westlake.edu.cn

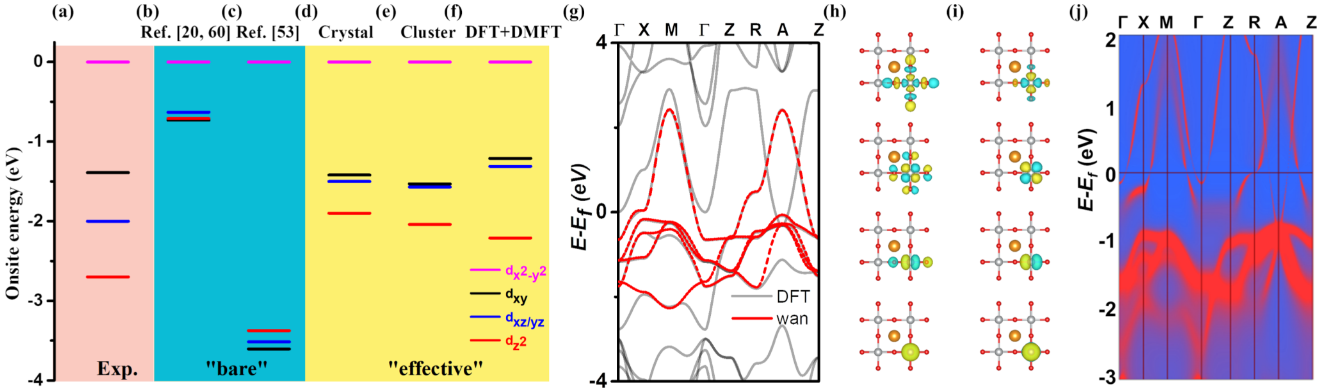

FIG. 1. Crystal field splitting for Ni 3*d* orbitals in infinite-layer nickelates. (a) Data from RIXS experiment [52]. The "bare" 3*d* orbital sequence from (b) Refs. [20,60] and (c) Ref. [53]. Onsite energies of "effective" 3*d* orbitals from (d) the crystal method (see text), (e) the cluster method, (f) DMFT calculation. (g) The density-functional theory (DFT) band structure and Wannier fitted effective bands within the crystal method. Maximally localized Wannier functions for (h) "effective" Ni 3*d* orbitals, compared with (i) "bare" Ni 3*d* and O 2*p* orbitals. (j) Momentum-resolved spectral function from DFT+DMFT calculations for $LaNiO_2$ at 116 K.

is, being a moderately correlated system, the combined effect of orbital-selective Mottness and Hundness makes nickelate-family a bridge connecting cuprates and iron pnictides.

II. FIRST-PRINCIPALS ANALYSIS

To construct a reliable microscopic model of nickelates, an accurate description of its crystal field splitting (CFS) is the first step, which will shed lights on its bonding nature and put strong constraints on the model. Recently, Rossi *et al.* [52] exploited the resonant inelastic x-ray scattering (RIXS) of nickelates and obtained an orbital sequence of $d_{x^2-y^2}$ (0 eV) > d_{xy} (−1.39 eV) > d_{xz}/d_{yz} (−2.0 eV) > d_{z^2} (−2.7 eV) [see Fig. 1(a)] by comparing the RIXS data with atomic multiple calculation. Although the role of Nd 5*d* cannot be excluded among the *dd* excitations, it is believed that the hybridization between Ni 3*d* and Nd 5*d* gives excitations with much smaller energy [52,60]. Therefore the above sequence reflects the CFS of Ni 3*d* orbitals. However, this significant observation cannot be simply explained by the "bare" Ni 3*d* orbitals (which are close to atomic orbitals) in previous first-principles calculations. For example, the result from Botana *et al.* [20] and Hepting *et al.* [60] is shown in Fig. 1(b) and that from Jiang *et al.* [53] is shown in Fig. 1(c), both of which significantly deviate from that shown in Fig. 1(a).

Due to such a disagreement between theory and experiment, we use three different methods to inspect the CFS in detail. First, the CFS is calculated through Wannier downfolding, dubbed the "crystal" method. Using five effective Ni 3*d* orbitals to fit the first-principles band structures [Fig. 1(g)], crucially, the obtained orbital sequence is consistent with experiment [Fig. 1(d)]. The spatial distribution of these Wannier functions (WFs) has contributions from both "bare" Ni 3*d* orbitals and O 2*p* orbitals [Fig. 1(h)]. Since the WFs carry more information from high-energy orbitals [61,62], the associated Wannier Hamiltonian is similar to an effective one. As a comparison, if more orbitals are included in the fitting process (see Fig. S2 and Fig. S3), the WFs are closer to atomic orbitals [Fig. 1(i)], making the associated Wannier Hamiltonian similar to a "bare" one. Second, the CFS is calculated through the cluster method [81] (please see details in Appendix A 3). The obtained sequence of "effective" orbitals (that are made of "bare" Ni 3*d* and O 2*p* orbitals) is also consistent with experiment [Fig. 1(e)]. Importantly, this method allows us to quantitatively analyze the components of effective orbitals. Taking $3d_{x^2-y^2}$ as an example, the weight of the O 2*p* orbital in this effective orbital of $NdNiO_2$ is ~23.8%, which is nearly half of that in $CaCuO_2$ (~44.8%) (see the Appendix). This analysis, complementarily with the "crystal" method, well explains the components of effective Ni 3*d* orbitals observed in experiment. Third, the CFS is calculated through density-functional theory (DFT)+dynamical mean-field theory (DMFT), which is comparable to a recent many-body quantum chemistry method [63]. Figure 1(j) shows the momentum-resolved spectral function of DFT+DMFT, where the extracted orbital sequence is $d_{x^2-y^2}$ (0 eV) > d_{xy} (−1.21 eV) > $d_{zx/zy}$ (−1.31 eV) > d_z^2 (−2.21 eV) [Fig. 1(f)]. This result not only has qualitatively the same sequence as but also is numerically close to the experiment [Fig. 1(a)]. Last, the above CFS can be understood in a simple picture. Due to D_{4h} symmetry of nickelates, the out-of-plane orbitals $\{d_{z^2}, d_{xz}, d_{yz}\}$ have lower energies by extending orbital along the *c* axis, leaving in-plane orbitals $\{d_{x^2-y^2}, d_{xy}\}$ more relevant to Fermi level [40], akin to the case in the infinite-layer cuprate $CaCuO_2$ (see the Appendix for more details).

The above three different methods give the same CFS with the experimental observations [52], indicating that the in-plane Ni $\{3d_{x^2-y^2}, 3d_{xy}\}$ orbitals are more relevant to the Fermi level. With these considerations, we propose a two-band microscopic model as:

$$\hat{H}_{\mathrm{TB}} = \sum_{i,\alpha,\sigma} \epsilon(\alpha)\hat{d}^{\dagger}_{i\alpha\sigma}\hat{d}_{i\alpha\sigma} + \sum_{\langle i,j\rangle,\alpha\sigma} [t(\alpha)\hat{d}^{\dagger}_{i\alpha\sigma}\hat{d}_{j\alpha\sigma} + \mathrm{H.c.}] + \sum_{\langle\langle i,j\rangle\rangle,\alpha\sigma} t'(\alpha)\hat{d}^{\dagger}_{i\alpha\sigma}\hat{d}_{j\alpha\sigma} + \mathrm{H.c.}$$

where σ is spin index, *i* and α is site- and orbital-index for $3d_{x^2-y^2}$ and $3d_{xy}$ WFs, and $\langle \ldots \rangle$ and $\langle\langle \ldots \rangle\rangle$ represent the

TABLE I. Two-band model parameter for RNiO$_2$ (R = La, Pr, Nd). $\epsilon(1)$ and $\epsilon(2)$ are onsite energy for $d_{x^2-y^2}$ and d_{xy} WFs. $t(1)$ and $t(2)$ [$t'(1)$ and $t'(2)$] are in-plane nearest- (next-nearest) neighbor hopping strength for $d_{x^2-y^2}$ and d_{xy} WFs. U (U') and J_H represent the intra- (inter-) orbital Coulomb repulsion and Hund's coupling.

R	$\epsilon(1)-\epsilon(2)$	$t(1)$	$t'(1)$	$t(2)$	$t'(2)$	U	U'	J_H
La	1.39	−0.37	0.10	−0.16	−0.05	3.60	1.90	0.84
Pr	1.41	−0.37	0.09	−0.16	−0.05	3.63	1.94	0.84
Nd	1.42	−0.37	0.09	−0.16	−0.05	3.64	1.95	0.84

nearest- and next-nearest-neighbor (NN and NNN) hopping. Since the $3d_{x^2-y^2}$ and $3d_{xy}$ are almost orthogonal to the rest $3d$ WFs, these model parameters are directly extracted from the crystal model (see the Appendix). The out-of-plane hopping value of $d_{x^2-y^2}$ (d_{xy}) WF is only 10% (20%) of its in-plane value, so the system shows a quasi-two-dimensional (2D) nature. Therefore, we consider only the hopping within the effective quasi-2D NiO$_2$ plane. As shown in Table I, both the NN and NNN hopping parameter of $d_{x^2-y^2}$ is two times larger than that of d_{xy}, giving an opportunity to see larger superexchange physics for $d_{x^2-y^2}$ orbital as we show below.

In order to investigate the interactions in nickelates, we consider the following Hamiltonian [10]:

$$\hat{H}_{\text{int}} = U\sum_{i,\alpha}\hat{n}_{i\alpha\uparrow}\hat{n}_{i\alpha\downarrow} + \sum_{i,\sigma,\sigma'}(U' - J_H\delta_{\sigma\sigma'})\hat{n}_{i1\sigma}\hat{n}_{i2\sigma'},$$

where U (U') denotes intra-(inter-)orbital Coulomb repulsion, and J_H denotes Hund's coupling. We take $U' = U - 2J_H$ so that the Hamiltonian is rotationally invariant in the orbital space. The U (U') and J_H on $3d$ WFs are estimated from the first-principles calculations with constrained random-phase approximation [64–66]. The interaction parameters for three nickelates are listed in Table I, showing the similar strength with well-kept relationship $U' = U - 2J_H$. The relatively large value of J_H therefore puts the infinite-layer nickelates as a moderate correlated system sharing similarity with iron-pnictides [67].

III. TWO WEAKLY INSULATORS

Having established the microscopic two-band Hubbard model with orbitals relevant to low-energy physics of nickelates, we first consider the evolution of its electronic structures on hole-doping. We introduce a slave-boson formalism [68,69] to decouple the exchange interactions, using a direct multiorbital generalization of original single-orbital scheme [70] (for details see the Appendix). Figures 2(a) and 2(b) presents the orbital-resolved charge density as a function of Hund's interaction (J_H) and doping ratio (x). We focus on $0 \leqslant x \leqslant 1$ that corresponds to the hole-doping evolution from $3d^9$ to $3d^8$ configuration on NiO$_2$ plane. The main feature is that there are three distinct phases depending on the strength of J_H versus η, called the orbital-selective Mottness regime, Hundness regime, and "mixed" regime. The Mottness (Hundness) phase occupies the small (large) J_H regime, while the mixed phase emerges in between. Figures 2(c) and 2(e) present the doping dependent orbital-resolved charge density (n_α) in three different regimes. In the orbital-selective Mottness regime [Fig. 2(c)], the doped-holes reside on Ni $3d_{x^2-y^2}$ orbital, and the Ni $3d_{xy}$ orbital is totally filled. Since a strong crystal field (η) favors a large orbital polarization, holes tend to fill the $3d_{x^2-y^2}$ orbital in a low-spin configuration. In the Hundness regime [see Fig. 2(e)], the doped-holes reside on the Ni $3d_{xy}$ orbital only. This is the result of a large Hund's exchange (J_H) promoting the carriers on different orbitals in a high-spin state to minimize repulsive interactions. Importantly, in the mixed phase [Fig. 2(d)], doping leads to a transition from Mottness to Hundness, where the holes reside on $3d_{x^2-y^2}$ orbital in the regime $x < x^*$, while the holes begin to populate $3d_{xy}$ orbital in the regime $x > x^*$. Here the critical value of x^* depends on J_H, η, i.e., the larger (smaller) J_H (η), the smaller value of x^*.

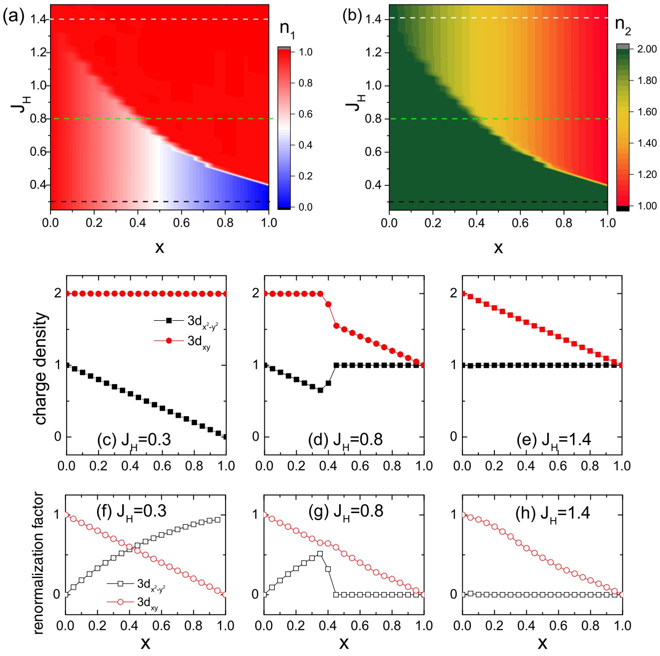

FIG. 2. Evolution of many-body electronic structure with hole-doping in the two-band Hubbard model. Density plot of orbital occupation on (a) Ni $3d_{x^2-y^2}$ orbital and (b) Ni $3d_{xy}$ orbital, as a function of Hund's interaction J_H and doping ratio x. Orbital charge density taken at specific Hund's interactions [dashed lines in (a) and (b)] are shown in the lower panels (c)–(e). [(f)–(h)] Orbital-resolved renormalization factor q_α (quasiparticle weight) as a function of x for (f) $J_H = 0.3$ eV, (g) $J_H = 0.8$ eV, and (h) $J_H = 1.4$ eV. Here we set $\eta = 1.2$ eV.

Furthermore, the competition between Hundness and Mottness can be revealed by the renormalization factor q_α (i.e., inverse of effective mass $\sim m_\alpha^{-1}$) of two bands, which qualifies the effective carrier quasiparticle weight, as shown in Fig. 2(f). In the orbital-selective Mottness regime, Ni $3d_{x^2-y^2}$ orbital is active and its quasiparticle weight increases as the hole-doping. In the Hundness regime [Fig. 2(h)], the $3d_{x^2-y^2}$ orbital is locked by Hund's interaction thus quasiparticle weight is pinned at exactly zero. In the mixed regime [Fig. 2(g)], $q_{x^2-y^2}$ exhibits a nonmonotonic behavior, with a maximum around $x \sim x^*$. After the Hundness physics sets in ($x > x^*$), $q_{x^2-y^2}$ drops to zero.

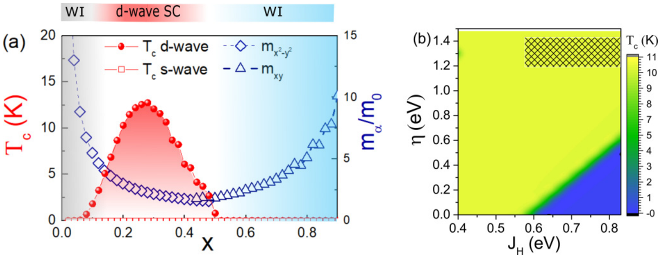

FIG. 3. Phase diagram on hole-doping, including d-wave SC and two weak insulators (WIs). (a) T_c versus doping ratio x for s-wave (red square) and d-wave (red dots) pairing symmetry, and effective mass m_α/m_0 for the $3d_{x^2-y^2}$ (blue diamond) and $3d_{xy}$ (blue triangular) orbitals. Here we set $J = 0.20$ eV, $J_H = 0.7$ eV, and $\eta = 1.2$ eV. (b) Heatmap of T_c versus J_H and η by setting $x = 0.2$, $J = 0.20$ eV. The shaded region marks parameters relevant to nickelates.

Here we stress that the "mixed" phase exhibits weakly insulating behavior in both lightly and heavily hole-doped regimes [Fig. 3(a)], but the origin of them is different. In the lightly hole-doped regime, the insulator comes from the suppressed kinetic mobility of carriers on $3d_{x^2-y^2}$ WF and vanishing small carrier density on $3d_{xy}$ WF. While in the heavily hole-doped regime, the insulating behavior is produced by frozen carriers on $3d_{x^2-y^2}$ and strong correlation due to Hundness. Thus, we conclude that the "mixed" phase induced by the competition between J_H and η leads to insulating behavior in both lightly and heavily hole-doped regimes, providing a natural understanding of experimental SC phase diagram.

In the phase diagram Fig. 3(a), in the overdoped regime, the $3d_{x^2-y^2}$ orbital becomes frozen and the $3d_{xy}$ orbital is active. In this case, even though the effective mass of the $3d_{xy}$ orbital could be moderated close to the superconductivity dome, the transport property contributed from $3d_{xy}$ orbital is inevitably influenced by the Hund effect, which should be different from the normal Fermi liquid theory for a single orbital.

IV. SUPERCONDUCTIVITY

Last, we turn to study the SC in our model. We assume the carrier pairing is mediated by the spin fluctuations, and additional antiferromagnetic interactions between the moment of charge carriers survive [30,71–73], $H_{\text{int}} = J\sum_{\langle ij\rangle,\alpha} \mathbf{S}_i \cdot \mathbf{S}_j - \frac{1}{4}n_i n_j$, where J denotes the effective spin exchange strength between the $3d_{x^2-y^2}$ orbitals. Then we treat this interaction at the mean-field level and self-consistently solve the pairing strength and critical temperature in the Bogoliubov-de Gennes (BdG) equations (see Appendix). Figure 3(a) shows the critical temperature T_c as a function of hole ratio. We find T_c of extended s-wave symmetry is vanishing small, and nonzero T_c is present for d-wave symmetry in the underdoped regime. That a SC dome appears sandwiched between orbital-selective Mott-insulator and Hund-induced correlated phase qualitatively agrees with the experimental observations.

To see the robustness of SC, other η and J_H values are studied here. Due to the screening effect from other $3d$ WFs, the realistic J_H between $3d_{x^2-y^2}$ and $3d_{xy}$ may deviate from the value listed in Table I up to 30%. And the three different models in determining CFS allows a reasonable window for η. In Fig. 3(b), it is clear the SC is stable in the parameter region relevant to nickelates [Fig. 3(b)]. In this regard we conclude the SC is robust and insensitive to the values of J_H, η.

V. CONCLUSION

Using comprehensive many-body computations based on a first-principles microscopic Hamiltonian, we present a unified physical picture for understanding the hole-doping superconducting phase diagram in infinite-layer nickelates [11–16,18] and provide a quantitative basis for theoretical models in describing the electronic structure revealed in RIXS [52]. Our study implies that infinite-layer nickelate-based superconductors, in a lightly hole-doped regime, are analogous to the cuprates with an active $3d_{x^2-y^2}$ orbital, resulting in Mottness physics. In contrast, in the heavily hole-doped regime, it shares many similarities with iron-based superconductors, such as the importance of Hund's interaction and tendency towards high-spin configurations. In this context, infinity-layer nickelate is a moderately correlated system in which the electronic structures of the NiO_2 layer bears similarities to those in either cuprates or iron-based materials in different regions.

Finally, we believe this work has implications on many aspects. First, the finding of a finite hybridization between O $2p$ orbitals and (bare) Ni $3d$ orbitals, akin to cuprates in the lightly doping regime, demonstrates the contribution from O $2p$ electrons cannot be totally neglected, thus pointing to a mixed charge-transfer and Mott characteristics for infinite-layer nickelates. It is able to explain a small but nonvanishing doping dependence of O K-edge spectra in the recent experiments [61,72]. Second, to further support the existence of a weak insulator in the overdoped regime, the hole-doped $Nd_6Ni_5O_{12}$ compound can be studied (undoped $Nd_6Ni_5O_{12}$ is equivalent to Ni $3d^{8.8}$ configuration [74,75]), and a weak insulator phase is expected in its heavily hole-doped regime. Last, important future problems include the exploration of possible enhancement of superconductivity in such a multi-orbital system and tuning superexchange effect via oxygen states would provide a practical route [62].

ACKNOWLEDGMENTS

W.Z. thanks H. H. Chen, J. H. Dai, M. Dean, R. H. He, K. Jiang, M. Jiang, Q. Y. Lu, F. Lechermann, C. A. Lane, Z. Ren, Q. H. Wang, X. G. Wan, C. J. Wu, J. Wu, Y. F. Yang, G. M. Zhang, and J. X. Zhu for discussion. W.Z. thanks M. R. Norman for critical comments and sharing his unpublished results. This work was supported by "Pioneer" and "Leading Goose" R&D Program of Zhejiang (2022SDXHDX0005), the Key R&D Program of Zhejiang Province (2021C01002) and the foundation from Westlake University. Z.F.W. was supported by NSFC (Grants No. 12174369 and No. 11774325), National Key Research and Development Program of China (Grant No. 2017YFA0204904) and Fundamental Research Funds for the Central Universities.

APPENDIX A: DENSITY-FUNCTIONAL THEORY AND DYNAMICAL MEAN-FIELD THEORY SIMULATIONS

In this Appendix, we provide some more numerical results to support the conclusions we have discussed in the main

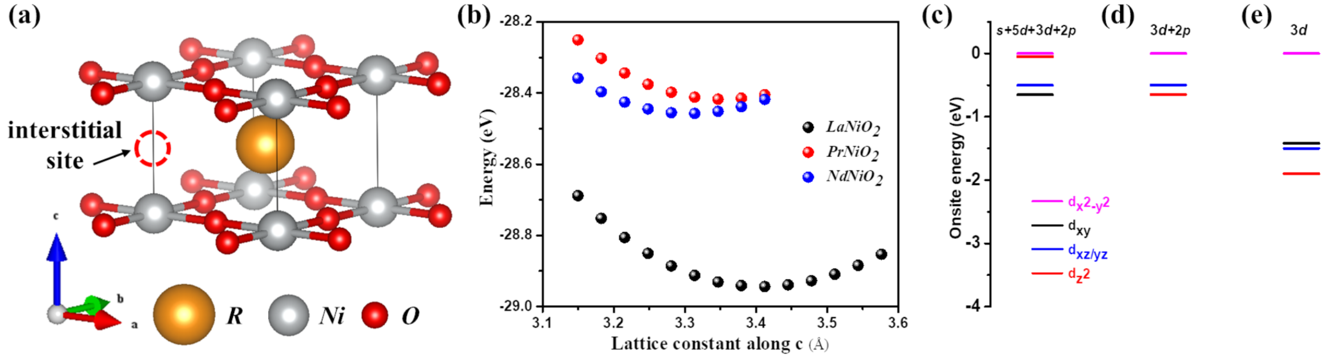

FIG. 4. (a) Archetype structure of $RNiO_2$, R = La, Pr, Nd. The interstitial site is marked by the red dashed circle. (b) Energy versus lattice constant in the c direction for $RNiO_2$. (c) Onsite energies of Ni $3d$ WFs when interstitial s, Nd $5d$, Ni $3d$, and O $2p$ orbitals are chosen in the downfolding. (d) Onsite energies of Ni $3d$ WFs when Ni $3d$ and O $2p$ orbitals are chosen in the downfolding. (e) Onsite energies of Ni $3d$ WFs when only Ni $3d$ orbitals are used in the downfolding. Here (e) is plotted for a clearer comparison.

text. In Appendix A, we present the computational details of density-functional theory and dynamical mean-field theory calculations and make a comparison with $CaCuO_2$. In Appendix B, we present an introduction of the slave-boson method for mean-field calculations. In Appendix C, we outline the Bogoliubov-de Gennes equation for superconductivity used in this work. In Appendix D, we provide further discussion to understand the contribution of R $5d$ electrons from a rare-earth element.

1. Crystal structure

DFT) calculations are performed within the plane wave, using the projector augmented wave method as implemented in the Vienna *ab initio* simulation package VASP [76–78]. The generalized gradient approximation was used for the exchange-correlation potential [79]. The infinite layered structure ABO_2 can be obtained from cubic perovskite ABO_3 by removing apical oxygen atoms [the left vacancy site is called interstitial site as shown in Fig. 4(a)]. To simulate the growth of $RNiO_2$ (R = La, Pr, Nd) layers on substrate $SrTiO_3$, the in-plane lattice constant of $RNiO_2$ is fixed to that of $SrTiO_3$ at 3.92 Å. The out-of-plane parameter is scanned to obtain the optimal value [the potential energy surface is shown in Fig. 4(b)], which is 3.41, 3.35, and 3.31 Å for $LaNiO_2$, $PrNiO_2$, and $NdNiO_2$. Because of the removal of apical O, the lattice constant in the c direction is much smaller than the in-plane lattice constants.

2. Wannier downfolding

To obtain parameters such as onsite energy and hopping integral, we downfold the full Hamiltonian into the subspace in Wannier90 package [80]. The downfolding process also allows us to obtain the following matrix element:

$$H_{\alpha\beta}(R) =< \phi_{0,\alpha}|\hat{H}|\phi_{R,\beta} >, \tag{A1}$$

where $|\phi_{0,\alpha} >$ is the maximally localized Wannier function α in home cell (index as 0) and $|\phi_{R,\beta} >$ the maximally localized Wannier function β in cell R. When R = 0, $\alpha = \beta$, the above matrix element orbital energy; otherwise, we obtain the hopping integral.

For example, the subspace can be chosen as interstitial s, Nd $5d$, Ni $3d$, and O $2p$ orbitals. There are 17 orbitals in total. The Wannier fitted band structure with respect to first-principles calculations is shown in Fig. 5(a) and the obtained WFs are displayed in Fig. 5(b). From Fig. 5(a), the fitted band structure is exactly the same as DFT in a very large energy window and WFs in Fig. 5(b) are very close to the corresponding atomic orbitals, so it is reasonable to call the Hamiltonian obtained here a “bare” one. (The real bare Hamiltonian should contain other bands including core levels, Ni $3s$, $3p$, and empty ones. These are quite high in energy and only renormalize the parameters by a small amount. Therefore it is safe to ignore these bands and call the Hamiltonian of 17 bands as bare Hamiltonian.) In this limit, the obtained onsite energy of Ni $3d$ WFs is shown in Fig. 4(c). As $\{3d_{x^2-y^2}, 3d_{z^2}\}$ and $\{3d_{xy}, 3d_{xz}, 3d_{yz}\}$ are almost degenerate, the Ni atoms now have coordination environments close to O_h spatial group.

We can reduce the number of bands in the downfolding, and then the contributions of these abandoned bands are projected to the kept subspace. Here we abandon higher-energy bands (interstitial s orbital and Nd $5d$), so the effective Hamiltonian now contains 11 bands: five Ni $3d$ and six O $2p$ WFs. The Wannier fitted band structure with respect to first-principles calculations is shown in Fig. 6(a) and the obtained WFs are displayed in Fig. 6(b). Since there is large interaction between Ni $3d_{z^2}$, interstitial s and Nd $5d_{z^2}$, the abandon of interstitial s and Nd $5d_{z^2}$ in the downfolding will be reflected on Ni $3d_{z^2}$ WF. As shown in Fig. 4(d), although the onsite energy of the other four $3d$ WFs does not change, the onsite energy of $3d_{z^2}$ is largely reduced and close to $3d_{xy}$.

Furthermore, in the downfolding process, we can construct “effective” (five) Ni $3d$ orbitals only, dubbed as the crystal model (compared with cluster method as shown below). In practice, this is equivalent to choosing subspace as (five) Ni $3d$ orbitals only in the Wannier downfolding. And the obtained on-site energy for Ni $3d$ orbitals is shown in Fig. 1(d) of the main text. One sees that the onsite energy of $3d_{z^2}$ is further reduced. Please note that the obtained orbitals contain contributions from both “bare” $3d$ orbitals and $2p$ orbitals, so that we call them “effective” orbitals to distinguish them from the “bare” ones.

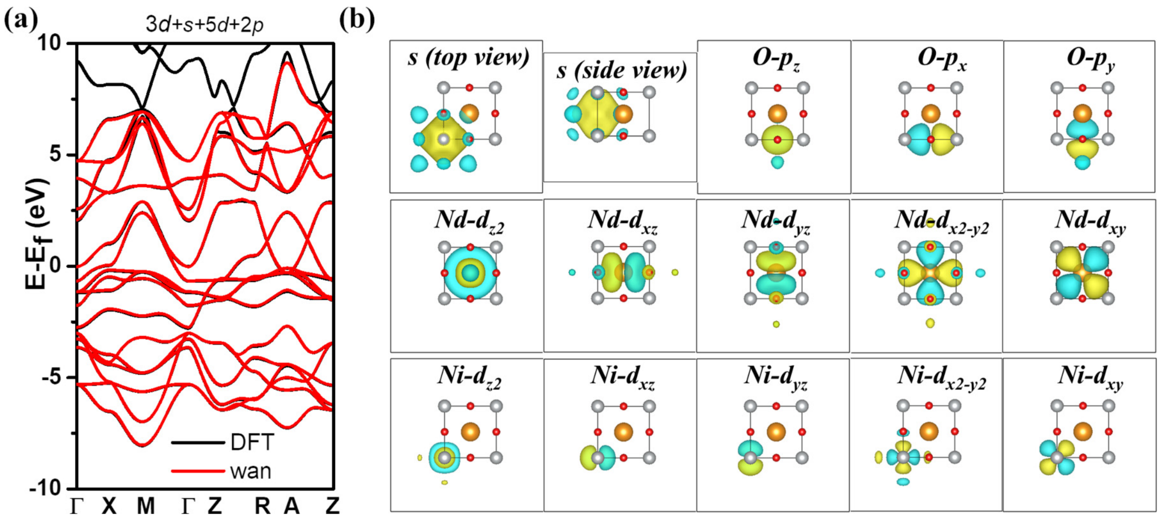

FIG. 5. Downfolding in the "bare" limit. (a) The DFT band structure and the Wannier fitted bands. (b) Maximally localized Wannier functions. The WFs on the other oxygen atoms is ignored here because of symmetry.

3. Cluster model calculation of 3*d* sequence

Based on the above band-structure calculations and Wannier downfolding scheme, here we can calculate the effective $3d$ orbital sequence (which is related to the RIXS experiment) through the cluster model proposed by Eskes *et al.* [81]. Here we consider a NiO$_4$ cluster: four O atoms forming a square and the Ni atom is at the center [see Fig. 7(a)]. We denote the bare on-site energy of $2p_i$ as $\epsilon(p_i)$ ($i = x, y, z$) and $3d_j$ as $\epsilon(d_j)$ ($j = z^2, x^2 - y^2, xy, xz, yz$). There are three steps for this treatment. At step 1, we start from the linear combination of p on the four O atoms according to the symmetry of $3d$ orbitals. Here we take the linear combination O1-p_x (also label as p_{x1}), O2-p_y, O3-p_x, and O4-p_y as an example [Fig. 7(a)]. Suppose the hopping between O1-p_x and O2-p_y is denoted by V_{pp} [V'_{pp} for O1-p_y and O2-p_x as displayed in Fig. 7(b)]. Now we consider their linear combinations; the resulting effective orbitals and onsite energies are easily calculated and the results are shown in Fig. 7(c). The bonding orbital is expressed as $\frac{1}{2}(p_{x_1} + p_{y_2} - p_{x_3} - p_{y_4})$ with onsite energy stabilized by $2|V_{pp}|$, so the onsite energy of this effective orbital is calculated as $\epsilon[\frac{1}{2}(p_{x_1} + p_{y_2} - p_{x_3} - p_{y_4})] = \epsilon(p_{x_1}) - 2|V_{pp}|$. The antibonding orbital is expressed as $\frac{1}{2}(p_{x_1} - p_{y_2} - p_{x_3} + p_{y_4})$ with onsite energy destabilized by by $2|V_{pp}|$, so the onsite energy is $\epsilon[\frac{1}{2}(p_{x_1} - p_{y_2} - p_{x_3} + p_{y_4})] = \epsilon(p_{x_1}) + 2|V_{pp}|$. The onsite energy of left two nonbonding orbitals do not change and is $\epsilon(p_{x_1})$.

At step 2, we consider the hopping between Ni $3d$ WFs and these effective orbitals formed by p. Here we take Ni $3d_{x^2-y^2}$ as an example. Suppose the hopping between O1-p$_x$ and $3d_{x^2-y^2}$ is $V_{x^2-y^2}$ as shown in Fig. 7(d); then the hopping between $3d_{x^2-y^2}$ and $\frac{1}{2}(p_{x_1} - p_{y_2} - p_{x_3} + p_{y_4})$ is given by $V = 0.5 * V_{x^2-y^2} * 4 = 2V_{x^2-y^2}$. The other symmetry-allowed hoppings are shown in Figs. 7(e)–7(g). Then we reach the information in Table II.

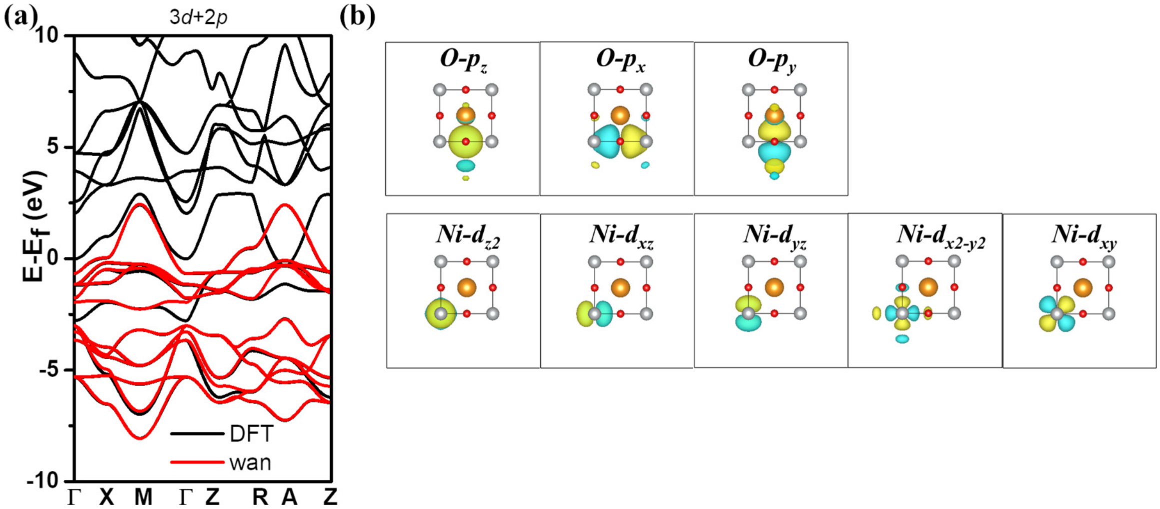

FIG. 6. Downfolding with Ni $3d$ and O $2p$ orbitals. (a) The DFT band structure and the Wannier fitted bands. (b) Maximally localized Wannier functions. The WFs on the other oxygen atoms is ignored here because of symmetry.

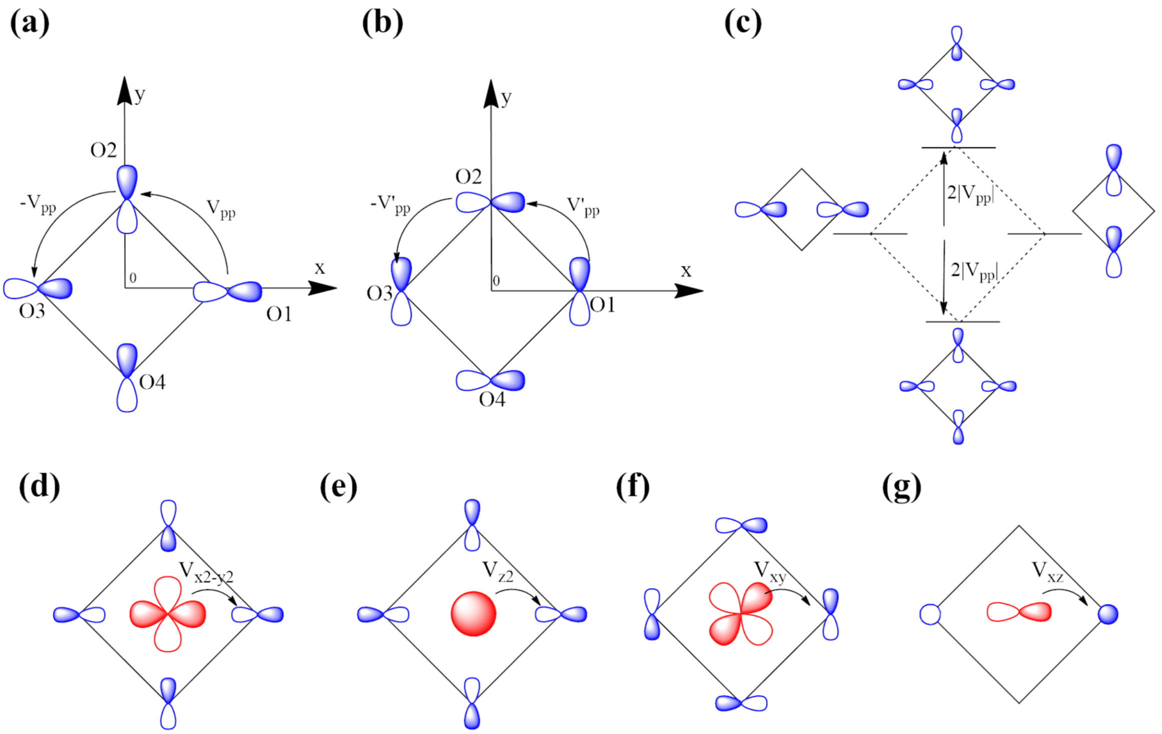

FIG. 7. NiO$_4$ cluster model. (a) The linear combination of O1-p_x, O2-p_y, O3-p_x, and O4-p_y. The hopping between O1-p_x and O2-p_y is V_{pp}. (b) The linear combination of O1-p_y, O2-p_x, O3-p_y, and O4-p_x. The hopping between O1-p_y and O2-p_x is V_{pp}. (c) Energy diagram for four effective p orbitals linear combined from O1-p_x, O2-p_y, O3-p_x, and O4-p_y. (d) Symmetry-allowed hopping between $3d_{x^2-y^2}$ and $\frac{1}{2}(p_{x_1} - p_{y_2} - p_{x_3} + p_{y_4})$. The hopping between $3d_{x^2-y^2}$ and p_{x_1} is $V_{x^2-y^2}$. (e) Symmetry-allowed hopping between $3d_{z^2}$ and $\frac{1}{2}(p_{x_1} + p_{y_2} - p_{x_3} - p_{y_4})$. The hopping between $3d_{z^2}$ and p_{x_1} is V_{z^2}. (f) Symmetry-allowed hopping between $3d_{xy}$ and $\frac{1}{2}(p_{y_1} + p_{x_2} - p_{y_3} - p_{x_4})$. The hopping between $3d_{xy}$ and p_{y_1} is V_{xy}. (f) Symmetry-allowed hopping between $3d_{xz}$ and $\frac{1}{\sqrt{2}}(p_{z_1} - p_{z_3})$. The hopping between $3d_{xz}$ and p_{z_1} is V_{xz}. Here d_{yz} and $\frac{1}{\sqrt{2}}(p_{z_2} - p_{z_4})$ is omitted for symmetry reason.

At step 3, we can construct a 2×2 matrix for each $3d$ and the corresponding effective p orbitals. Diagonalizing the matrix gives two eigenvalues. Since the effective p orbitals have lower onsite energies than $3d$, the higher eigenvalue gives the onsite energy of related effective $3d$ orbitals. For NdNiO$_2$, the parameters from the above downfolding are $\epsilon(d_{x^2-y^2}) = 5.57$ eV, $\epsilon(d_{z^2}) = 4.93$ eV, $\epsilon(d_{xy}) = 4.92$ eV, $\epsilon(d_{xz}) = 5.06$ eV, $\epsilon(p_{x_1}) = 1.19$ eV, $\epsilon(p_{y_1}) = 1.91$ eV, $\epsilon(p_{z_1}) = 1.96$ eV, $V_{pp} = -0.62$ eV, $V'_{pp} = -0.26$ eV, $V_{x^2-y^2} = 1.28$ eV, $V_{z^2} = -0.19$ eV, $V_{xy} = -0.75$ eV, and $V_{xz} = -0.80$ eV, which gives the effective $3d$ sequence as $d_{x^2-y^2}$ (0 eV) > d_{xy} (−1.53 eV) > d_{xz}/d_{yz} (−1.57 eV) > d_{z^2} (−2.04 eV). This is shown in Fig. 1(e).

Importantly, the cluster method can also infer the information on the effective $3d$ orbitals. Here we compare the NiO$_4$ cluster from NdNiO$_2$ and the CuO$_4$ cluster from CaCuO$_2$ (see Appendix A 6 for more information). As shown in Table III, CaCuO$_2$ is a typical charge-transfer insulator and the contribution from O $2p$ orbitals is close to 50%, except for d_{z^2} effective orbitals. But the $2p$ contributions are much smaller in NiO$_4$, and here we take effective $3d_{x^2-y^2}$ orbitals as an example. We see the weight of O $2p$ in this effective orbital of NdNiO$_2$ is around 23.8%. As a comparison, we find the weight of O $2p$ orbital in CaCuO$_2$ is around 44.8%. Thus, the component of O p orbital in NiO$_4$ is only half of that in CuO$_4$. This is one of key difference between NdNiO$_2$ and CaCuO$_2$. This difference is able to explain that, in the recent EELS experiment [61], hole-doping only leads to a relatively small change of the O K-edge XAS spectrum in NdNiO$_2$ compared to cuprates.

4. Impurity model calculation of 3*d* sequence

DFT+DMFT provides an impurity model approach towards the $3d$ orbital sequence. We have performed calcula-

TABLE II. Cluster model parameter. Here d_{yz} and $\frac{1}{\sqrt{2}}(p_{z_2} - p_{z_4})$ is omitted for symmetry.

State	$\epsilon(d)$	ϵ(effective p)	Hopping
$\{d_{x^2-y^2}, \frac{1}{2}(p_{x_1} - p_{y_2} - p_{x_3} + p_{y_4})\}$	$\epsilon(d_{x^2-y^2})$	$\epsilon(p_{x_1}) + 2V_{pp}$	$2V_{x^2-y^2}$
$\{d_{z^2}, \frac{1}{2}(p_{x_1} + p_{y_2} - p_{x_3} - p_{y_4})\}$	$\epsilon(d_{z^2})$	$\epsilon(p_{x_1}) - 2V_{pp}$	$2V_{z^2}$
$\{d_{xy}, \frac{1}{2}(p_{y_1} + p_{x_2} - p_{y_3} - p_{x_4})\}$	$\epsilon(d_{xy})$	$\epsilon(p_{y_1}) - 2V'_{pp}$	$2V_{xy}$
$\{d_{xz}, \frac{1}{\sqrt{2}}(p_{z_1} - p_{z_3})\}$	$\epsilon(d_{xz})$	$\epsilon(p_{z_1})$	$\sqrt{2}V_{xz}$

TABLE III. The weight of O p orbital in each effective $3d$ orbitals in NiO_4 cluster from $NdNiO_2$ compared with CuO_4 cluster from $CaCuO_2$. Here $d_{yz} - \frac{1}{\sqrt{2}}(p_{z_2} - p_{z_4})$ is omitted for symmetry.

O p weight	$d_{x^2-y^2} - \frac{1}{2}(p_{x_1} - p_{y_2} - p_{x_3} + p_{y_4})$	$d_{z^2} - \frac{1}{2}(p_{x_1} + p_{y_2} - p_{x_3} - p_{y_4})$	$d_{xy} - \frac{1}{2}(p_{y_1} + p_{x_2} - p_{y_3} - p_{x_4})$	$d_{xz} - \frac{1}{\sqrt{2}}(p_{z_1} - p_{z_3})$
NiO_4	23.8%	0.6%	11.9%	9.6%
CuO_4	44.8%	3.3%	43.7%	45.2%

tions with $LaNiO_2$ and $NdNiO_2$. In both compounds, Ni-$3d$ orbitals are considered correlated impurities. In addition, for $NdNiO_2$, two different methodologies are employed for Nd-$4f$ orbitals, namely (1) open-core treatment and (2) correlated impurity on the equal-footing as Ni-$3d$. For each case, we have performed calculations using both $U_d = 5.0$ eV, $J_d = 0.8$ eV and $U_d = 6.0$ eV, $J_d = 0.9$ eV (see Fig. 8). For the realistic Nd calculations, $U_f = 6.0$ eV, $J_f = 0.7$ eV is employed for Nd-$4f$ orbitals as well. In all calculations, the continuous time quantum Monte Carlo (CTQMC) impurity solver is employed. The solver samples 2×10^9 steps at 116K. The nominal double-counting scheme was employed in these calculations, with $n_d = 9.0$.

We show the crystal field splitting obtained from DFT+DMFT calculations in Table IV. In all cases, the low-energy effective crystal field splitting has the same order as experimental observation. Here we conclude the DMFT calculations give consistent results about the Ni $3d$ sequence.

5. *3d* sequence in $CaCuO_2$

To make a comparison with cuprates, here we consider the infinite-layer cuprate $CaCuO_2$ [82]. The lattice constant we use is $a = b = 3.90$ Å and $c = 3.21$ Å. The result is shown in Fig. 9. Here the experimental result [Fig. 9(a)] is taken from Hozoi *et al.* [83], which the contribution of magnetic contributions are excluded [84]. The CFS of the crystal model is shown in Fig. 9(b), which is almost the same to the experimental date in Fig. 9(a). The Wannier fitted band structure with respect to first-principles calculation is shown in Fig. 9(e) and the obtained WFs are shown in Fig. 9(f), with large tails on the nearby O atoms. We can also use both Cu $3d$ and O $2p$ in the downfolding. Once the O $2p$ orbitals are used, the the hybridization of O $2p$ and Cu $3d$ is closed and the WFs resembles atomic $3d$ orbitals [compare Fig. 9(g) and Fig. 9(f)]. The parameters from such downfolding in $CaCuO_2$ are follows: $\epsilon(d_{x^2-y^2}) = 2.38$ eV, $\epsilon(d_{z^2}) = 1.90$ eV, $\epsilon(d_{xy}) = 1.87$ eV, $\epsilon(d_{xz}) = 1.96$ eV, $\epsilon(p_{x_1}) = 0.59$ eV, $\epsilon(p_{y_1}) = 1.90$ eV, $\epsilon(p_{z_1}) = 1.76$ eV, $V_{pp} = -0.64$eV, $V'_{pp} = -0.47$ eV, $V_{x^2-y^2} = 1.22$ eV, $V_{z^2} = -0.25$ eV, $V_{xy} = -0.68$ eV, $V_{xz} = -0.72$ eV, which allows us to calculate effective $3d$ sequence through cluster model as $d_{x^2-y^2}$ (0 eV) > d_{xy} (−1.66 eV) > d_{xz}/d_{yz} (−1.70 eV) > d_{z^2} (−2.58 eV). This is shown in Fig. 9(c).

Hozoi *et al.* [83] has applied state-of-art many-body quantum chemistry methods (CASSCF+SDCI) to study the CFS and the obtained orbital order is shown in Fig. 9(d). Therefore, all three models give a consistent CFS of Cu $3d$ effective orbitals.

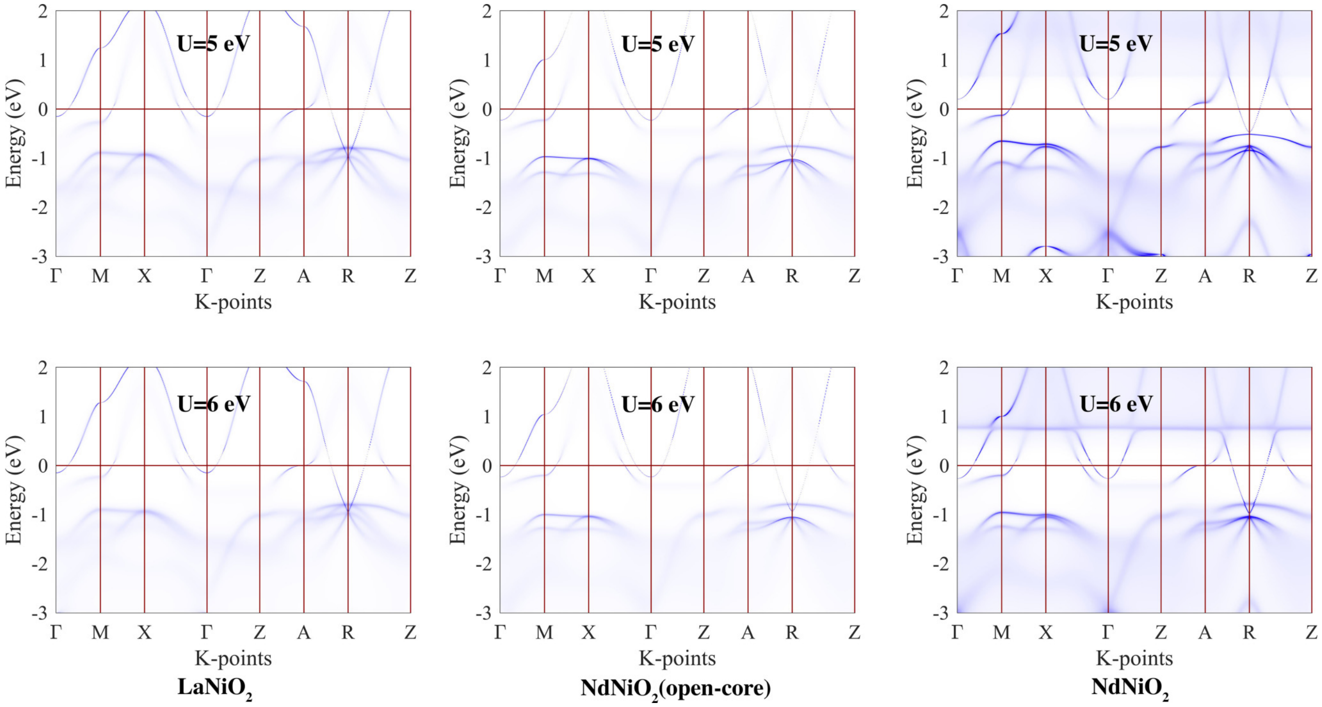

LaNiO$_2$ **NdNiO$_2$(open-core)** **NdNiO$_2$**

FIG. 8. Momentum-resolved spectral function from DFT+DMFT calculations for $LaNiO_2$ and $NdNiO_2$ at 116 K.

TABLE IV. CFS obtained in DFT+DMFT calculations. In NdNiO$_2$ calculations, Nd-4f orbitals are treated using open-core method [column NdNiO$_2$ (opencore)] or on the equal footing using CTQMC [column NdNiO$_2$ (full)]. All orbital energies are relative to $d_{x^2-y^2}$ orbitals, and all units are in eV. In each column, the left number is the "bare" result, where the self-energy takes the infinity frequency limit [$\Sigma(\omega \rightarrow \infty)$] and only statically shifts the DFT levels, while the right column is the "interacting" result, where the zero-frequency limit [$\Sigma(\omega = 0)$], representing the renormalized quasiparticle result.

	LaNiO$_2$				NdNiO$_2$ (opencore)				NdNiO$_2$ (full)			
	$U = 5.0$		$U = 6.0$		$U = 5.0$		$U = 6.0$		$U = 5.0$		$U = 6.0$	
$d_{x^2-y^2}$	0.0		0.0		0.0		0.0		0.0		0.0	
d_{xy}	−0.47	−1.17	−0.48	−1.21	−0.60	−1.28	−0.60	−1.30	−0.60	−1.23	−0.61	−1.25
$d_{zx/zy}$	−0.13	−1.28	−0.13	−1.31	−0.29	−1.33	−0.29	−1.35	−0.17	−1.27	−0.16	−1.27
d_{z^2}	0.15	−2.15	0.17	−2.21	0.10	−2.05	0.12	−2.08	0.11	−1.96	0.13	−1.96

6. Physical picture for the crystal field splitting

In the main text, we have shown numerical results and detailed discussion on the crystal field splitting of Ni 3d orbitals. Here we provide a physical picture to understand this result.

A vast of band structure calculations have shown a multiband nature around the Fermi level [20–23,40–50,53–59]. In addition to the Ni 3$d_{x^2-y^2}$ band, most works [41–50] prefer to use 3d_{z^2} as the other target orbital based on the following two reasons: (1) 3d_{z^2} contributes the Γ electron pocket and (2) it is analogous to cuprates where the 3d_{z^2}orbital is closest to 3$d_{x^2-y^2}$. However, different from cuprates with O_h symmetry, the point group of nickelates is reduced to D_{4h}, and thus the crystal field splitting should be different. In Fig. 10, we present a diagram to understand the crystal field splitting under the change of tetragonal distortion along the c direction. In contrast to O_h symmetry, by removing the apical O, the out-of-plane orbitals $\{d_{z^2}, d_{xz}, d_{yz}\}$ have lower energies by extending the orbital along the c axis, leaving in-plane orbitals $\{d_{x^2-y^2}, d_{xy}\}$ relevant to the Fermi level [40]. This applies to both infinite-layer CaCuO$_2$ and NdNiO$_2$. This also explains why the out-of-plane 3d_{z^2} is considerably lower in energy compared to the degenerate 3d_{xy}, 3$d_{xz/yz}$ levels, contrary to the commonly accepted crystal field picture for a square planar coordination.

7. Parameters of the two-band model

As Ni 3d_{xy} is orthogonal to both NN and NNN 3d_{xz}, 3d_{yz}, 3d_{z^2} and 3$d_{x^2-y^2}$, 3$d_{x^2-y^2}$ is orthogonal to NN and NNN 3d_{xz}, 3d_{yz}, 3d_{xy}, with negligible hopping to NN 3d_{z^2} (0.023 eV) and orthogonal to NNN 3d_{z^2}, the $\{3d_{xy}, 3d_{x^2-y^2}\}$ can be regarded as orthogonal to $\{3d_{xz}, 3d_{yz}, 3d_{z^2}\}$. This allows us to separate $\{3d_{xy}, 3d_{x^2-y^2}\}$ out, which means we can directly extract the parameters related to $\{3d_{xy}, 3d_{x^2-y^2}\}$ from the crystal model. The obtained parameters are listed in Table I in the main text. With these parameters, we can recalculate the band structure as shown in Fig. 11. The good agreement between these two indicates the validity of the model parameters.

APPENDIX B: SLAVE-BOSON MEAN-FIELD CALCULATION

We use the slave-boson mean-field method to deal with the interaction between electrons. The slave-boson mean-field method was first introduced to describe the unoccupied states [85,86]. Then Kotliar and Ruckenstein extended the slave-boson formalism, and they used four slave-bosons to describe four different occupied states on one site [68,69]. In this way, the Hubbard interaction term can be mapped to slave-boson space and simply expressed by slave-boson operators, and simultaneously the hopping terms are also modified.

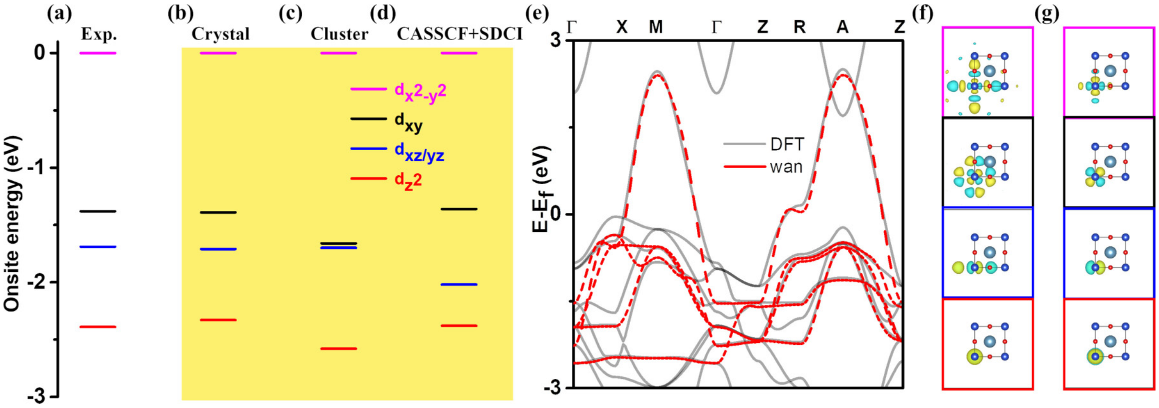

FIG. 9. Onsite energy for the Cu 3d orbital. (a) From experimental data [83]; (b) from crystal model; (c) from cluster model; (d) from state-of-the-art many-body quantum chemistry method data. The onsite energy of $d_{x^2-y^2}$ is set to be zero [83]. (e) The DFT band structure and the Wannier fitted effective bands with Cu 3d orbitals. Maximally localized wannier functions for (f) Cu 3d orbital only and (g) Cu 3d orbitals and O 2p orbitals used in the downfolding process.

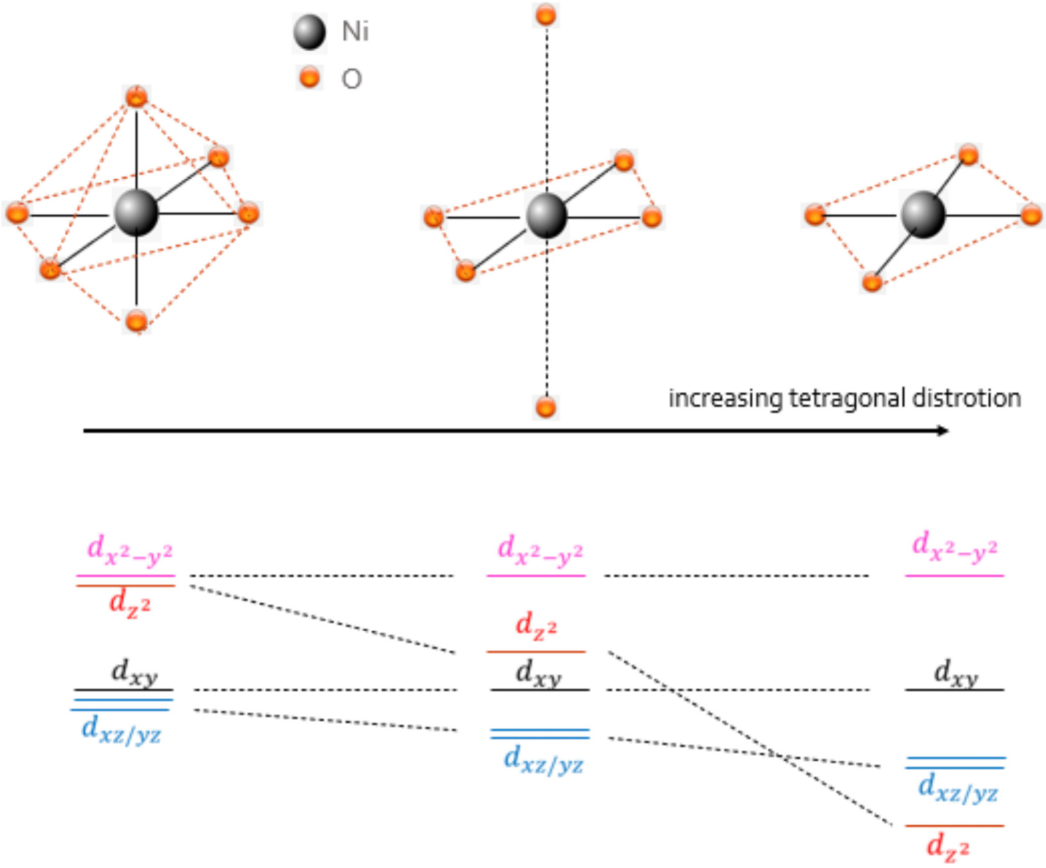

FIG. 10. Schematic plot of crystal field splitting by increasing tetragonal distortion along the c axis. Different $3d$ orbitals are labeled by colors.

In this paper, we use a two-orbital slave-boson method to deal with interaction term [70]. First, we introduce 16 slave-boson operators to describe 16 different occupied states on each site,

$$\{e^{(\dagger)}, p_{\alpha\sigma}^{(\dagger)}, s_{\alpha}^{(\dagger)}, d_{\sigma\sigma'}^{(\dagger)}, h_{\alpha\sigma}^{(\dagger)}, f^{(\dagger)}\}, \tag{B1}$$

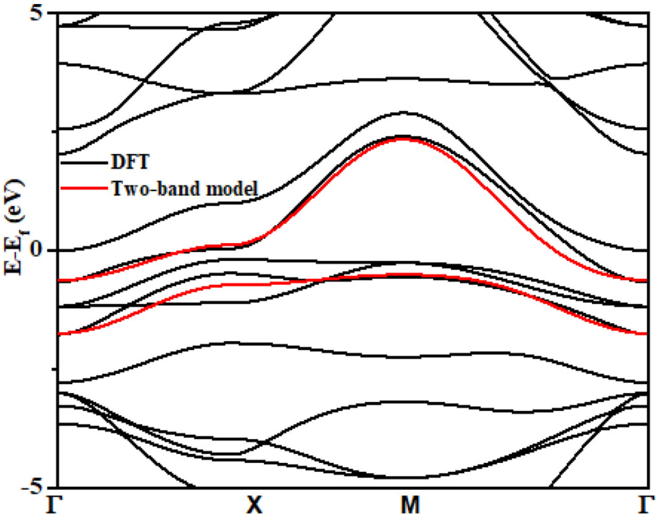

FIG. 11. Band structure of two-band model and first-principles calculation for NdNiO$_2$. Here a 2D Brillouin zone is used and the band structure of the two-band model is shifted.

where $\alpha = 1, 2$ (label $d_{x^2-y^2}$ and d_{xy}, respectively) is the band index and $\sigma =\uparrow, \downarrow$ is the spin index. These 16 slave-boson states have been listed in Table V. The introduction of 16 slave-bosons enlarge the Hilbert space to an unphysical one, so we need some local constraints to form a physical space. Summing up all slave-boson operators, we define

$$\begin{aligned}\hat{I}_i = {} & e_i^\dagger e_i + \sum_{\alpha\sigma}(p_{i\alpha\sigma}^\dagger p_{i\alpha\sigma} + h_{i\alpha\sigma}^\dagger h_{i\alpha\sigma}) + \sum_{\alpha} s_{i\alpha}^\dagger s_{i\alpha} \\ & + \sum_{\sigma\sigma'} d_{i\sigma\sigma'}^\dagger d_{i\sigma\sigma'} + f_i^\dagger f_i,\end{aligned} \tag{B2}$$

TABLE V. The atomic states in the original model, their corresponding slave-boson states, as well as the labeling of the mean fields. The site index is suppressed, $\alpha = 1, 2$, and $\bar{\sigma} =\downarrow (\uparrow)$ if $\sigma =\uparrow (\downarrow)$ [70].

	Original model	Slave-boson model	Mean fields
$\lvert e\rangle$	$\lvert 0\rangle$	$e^\dagger\lvert\text{vac}\rangle$	$e \equiv \langle e^{(\dagger)}\rangle$
$\lvert p_{\alpha\sigma}\rangle$	$\hat{d}_{\alpha\sigma}^\dagger\lvert 0\rangle$	$p_{\alpha\sigma}^\dagger\hat{d}_{\alpha\sigma}^\dagger\lvert\text{vac}\rangle$	$p_{\alpha\sigma} \equiv \langle p_{\alpha\sigma}^{(\dagger)}\rangle$
$\lvert s_\alpha\rangle$	$\hat{d}_{\alpha\uparrow}^\dagger\hat{d}_{\alpha\downarrow}^\dagger\lvert 0\rangle$	$s_\alpha^\dagger\hat{d}_{\alpha\uparrow}^\dagger\hat{d}_{\alpha\downarrow}^\dagger\lvert\text{vac}\rangle$	$s_\alpha \equiv \langle s_\alpha^{(\dagger)}\rangle$
$\lvert d_{\sigma\sigma}\rangle$	$\hat{d}_{1\sigma}^\dagger\hat{d}_{2\sigma}^\dagger\lvert 0\rangle$	$d_{\sigma\sigma}^\dagger\hat{d}_{1\sigma}^\dagger\hat{d}_{2\sigma}^\dagger\lvert\text{vac}\rangle$	$d_{\sigma\sigma} \equiv \langle d_{\sigma\sigma}^{(\dagger)}\rangle$
$\lvert d_{\sigma\bar{\sigma}}\rangle$	$\hat{d}_{1\sigma}^\dagger\hat{d}_{2\bar{\sigma}}^\dagger\lvert 0\rangle$	$d_{\sigma\bar{\sigma}}^\dagger\hat{d}_{1\sigma}^\dagger\hat{d}_{2\bar{\sigma}}^\dagger\lvert\text{vac}\rangle$	$d_{\sigma\bar{\sigma}} \equiv \langle d_{\sigma\bar{\sigma}}^{(\dagger)}\rangle$
$\lvert h_{1\sigma}\rangle$	$\hat{d}_{1\sigma}^\dagger\hat{d}_{2\uparrow}^\dagger\hat{d}_{2\downarrow}^\dagger\lvert 0\rangle$	$h_{1\sigma}^\dagger\hat{d}_{1\sigma}^\dagger\hat{d}_{2\uparrow}^\dagger\hat{d}_{2\downarrow}^\dagger\lvert\text{vac}\rangle$	$h_{1\sigma} \equiv \langle h_{1\sigma}^{(\dagger)}\rangle$
$\lvert h_{2\sigma}\rangle$	$\hat{d}_{1\uparrow}^\dagger\hat{d}_{1\downarrow}^\dagger\hat{d}_{2\sigma}^\dagger\lvert 0\rangle$	$h_{2\sigma}^\dagger\hat{d}_{1\uparrow}^\dagger\hat{d}_{1\downarrow}^\dagger\hat{d}_{2\sigma}^\dagger\lvert\text{vac}\rangle$	$h_{2\sigma} \equiv \langle h_{2\sigma}^{(\dagger)}\rangle$
$\lvert f\rangle$	$\hat{d}_{1\uparrow}^\dagger\hat{d}_{1\downarrow}^\dagger\hat{d}_{2\uparrow}^\dagger\hat{d}_{2\downarrow}^\dagger\lvert 0\rangle$	$f^\dagger\hat{d}_{1\uparrow}^\dagger\hat{d}_{1\downarrow}^\dagger\hat{d}_{2\uparrow}^\dagger\hat{d}_{2\downarrow}^\dagger\lvert\text{vac}\rangle$	$f \equiv \langle f^{(\dagger)}\rangle$

and define the operators,

$$\hat{Q}_{i1\sigma} = p^{\dagger}_{i1\sigma} p_{i1\sigma} + s^{\dagger}_{i1} s_{i1} + \sum_{\sigma'} d^{\dagger}_{i\sigma\sigma'} d_{i\sigma\sigma'} + h^{\dagger}_{i1\sigma} h_{i1\sigma} + \sum_{\sigma} h^{\dagger}_{i2\sigma} h_{i2\sigma} + f^{\dagger}_{i} f_{i}, \tag{B3}$$

$$\hat{Q}_{i2\sigma} = p^{\dagger}_{i2\sigma} p_{i2\sigma} + s^{\dagger}_{i2} s_{i2} + \sum_{\sigma'} d^{\dagger}_{i\sigma'\sigma} d_{i\sigma'\sigma} + h^{\dagger}_{i2\sigma} h_{i2\sigma} + \sum_{\sigma} h^{\dagger}_{i1\sigma} h_{i1\sigma} + f^{\dagger}_{i} f_{i}. \tag{B4}$$

Thus, the physical subspace is given by two kinds local constraints:

$$\hat{I}_i - 1 \equiv 0, \tag{B5}$$

$$\hat{f}^{\dagger}_{i\alpha\sigma} \hat{f}_{i\alpha\sigma} - \hat{Q}_{i\alpha\sigma} \equiv 0. \tag{B6}$$

These constraints ensure a physical local Hilbert space of the slave-boson model. The first relation (B5) represents the completeness of the boson operators, i.e., the total probability of slave-bosons on one site is 1. The second relation (B6) is similar to the conservation of the number of particles, i.e., the charge of bosons should be equal to the electron number. Therefore, we have to ensure that in the physical subspace the operators $\hat{Q}_{i\alpha\sigma}$ are identical to the operators $\hat{f}^{\dagger}_{i\alpha\sigma}\hat{f}_{i\alpha\sigma}$. Using these constraints and neglecting the spin-flip and pair-hopping term in Hund coupling, the interaction term becomes quadratic in the boson operators:

$$\hat{H}_{\text{int}} = \sum_{i} \Bigg\{ U \sum_{\alpha} s^{\dagger}_{i\alpha} s_{i\alpha} + (U + 2U' - J_H) \sum_{\alpha\sigma} h^{\dagger}_{i\alpha\sigma} h_{i\alpha\sigma} + (U' - J_H) \sum_{\sigma} d^{\dagger}_{i\sigma\sigma} d_{i\sigma\sigma} + U' \sum_{\sigma} d^{\dagger}_{i\sigma\bar{\sigma}} d_{i\sigma\bar{\sigma}} + 2(U + 2U' - J_H) f^{\dagger}_{i} f_{i} \Bigg\}. \tag{B7}$$

But the hopping term become more complex by the correction of slave-bosons. There is a mapping for the hopping term:

$$\hat{d}_{i\alpha\sigma} \rightarrow \tilde{z}_{i\alpha\sigma} \hat{d}_{i\alpha\sigma}, \quad \hat{d}^{\dagger}_{i\alpha\sigma} \rightarrow \hat{d}^{\dagger}_{i\alpha\sigma} \tilde{z}^{\dagger}_{i\alpha\sigma}, \tag{B8}$$

where

$$\begin{aligned} \tilde{z}_{i\alpha\sigma} &= (1 - \hat{Q}_{i\alpha\sigma})^{-1/2} z_{i\alpha\sigma} \hat{Q}^{-1/2}_{i\alpha\sigma} \\ z_{i1\sigma} &= e^{\dagger}_{i} p_{i1\sigma} + p^{\dagger}_{i1\bar{\sigma}} s_{i1} + p^{\dagger}_{i2\sigma} d_{i\sigma\sigma} + p^{\dagger}_{i2\bar{\sigma}} d_{i\sigma\bar{\sigma}} \\ &\quad + s^{\dagger}_{i2} h_{i1\sigma} + d^{\dagger}_{i\bar{\sigma}\sigma} h_{i2\sigma} + d^{\dagger}_{i\bar{\sigma}\bar{\sigma}} h_{i2\bar{\sigma}} + h^{\dagger}_{i1\bar{\sigma}} f_i \\ z_{i2\sigma} &= e^{\dagger}_{i} p_{i2\sigma} + p^{\dagger}_{i2\bar{\sigma}} s_{i2} + p^{\dagger}_{i1\sigma} d_{i\sigma\sigma} + p^{\dagger}_{i1\bar{\sigma}} d_{i\bar{\sigma}\sigma} \\ &\quad + s^{\dagger}_{i1} h_{i2\sigma} + d^{\dagger}_{i\sigma\bar{\sigma}} h_{i1\sigma} + d^{\dagger}_{i\bar{\sigma}\bar{\sigma}} h_{i1\bar{\sigma}} + h^{\dagger}_{i2\bar{\sigma}} f_i. \end{aligned} \tag{B9}$$

The z operators keep track of the slave-bosons during the hopping processes and the choice of the z operators is not unique. In our paper, the hopping term can be written as:

$$\hat{H}_{\text{TB}} = \sum_{i,\alpha,\sigma} \epsilon_{\alpha} \hat{n}_{i\alpha\sigma} + \sum_{\langle i,j\rangle,\alpha,\sigma} (t_{\alpha} \hat{f}^{\dagger}_{i\alpha\sigma} \tilde{z}^{\dagger}_{i\alpha\sigma} \tilde{z}_{j\alpha\sigma} \hat{f}_{j\alpha\sigma} + \text{H.c.}) \tag{B10}$$

Only the hopping term is corrected here, and the on-site energy is unchanged. The saddle-point approximation is equivalent to a mean-field approximation where the Bose fields and Lagrange multipliers are treated as static and homogeneous fields [68–70]. Thus, this approximation consists essentially in replacing the creation and annihilation operators of the slave-bosons by site-independent c numbers which can be chosen to be real. So the interaction term is only dependent on these c numbers:

$$\begin{aligned} H_{\text{int}} &= NU\left(s_1^2 + s_2^2\right) + N(U + 2U' - J_H)\left(h^2_{1\uparrow} + h^2_{1\downarrow} + h^2_{2\uparrow} + h^2_{2\downarrow}\right) \\ &\quad + N(U' - J_H)\left(d^2_{\uparrow\uparrow} + d^2_{\downarrow\downarrow}\right) + NU'\left(d^2_{\uparrow\downarrow} + d^2_{\downarrow\uparrow}\right) \\ &\quad + 2N(U + 2U' - J_H) f^2. \end{aligned} \tag{B11}$$

We define a new factor $q_{\alpha\sigma} =< \tilde{z}^{\dagger}_{\alpha\sigma} \tilde{z}_{\alpha\sigma} >$ to describe the correction of the hopping term. In our choice, the q factor is defined as a real number from 0 to 1. As Hubbard interaction strength increases, the q factors decrease. If the band is half-filling, then the q factor will become zero, which means a Mott insulator. The hopping term can be written as

$$\hat{H}_{\text{TB}} = \sum_{i,,\sigma} \epsilon_{\alpha} \hat{n}_{i\alpha\sigma} + \sum_{<i,j>,\alpha,\sigma} (t_{\alpha} q_{\alpha\sigma} \hat{d}^{\dagger}_{i\alpha\sigma} \hat{d}_{j\alpha\sigma} + \text{H.c.}). \tag{B12}$$

It can be easily seen that the role of the slave-bosons is to renormalize the electronic hopping strength. The c numbers of the slave-bosons can be solved by minimization of free energy. Next, we need to simplify our model, because the 16 slave-boson parameters are not easy to solve, even on the mean-field level. Let us analyze the real situation of our system. In our system, when we consider Ni $3d_{x^2-y^2}$ and $3d_{xy}$ orbitals, the electron on every site is between 2 and 3. Moreover, there is a large crystal field split between two orbitals. And the Hubbard interaction strength U in two orbits is very large, which prevents two electrons from occupying the same orbit on the same site. In addition, we assume that system is spin degenerate. So we believe that the probability of some electron occupied states is very small, such as empty, single, and four occupied states, and these states can be ignored in our case, so it is only four effective occupied states are left in our model, and they are $\{s, d_1, d_2, h_1\}$. s means there are two electrons in the lower band ($s = s_2$). d_1 means the each band has one electron ($d_1 = d_{\uparrow\uparrow} = d_{\downarrow\downarrow}$), and the two electrons are arranged paramagnetically. Relatively, d_2 means two electrons are antiferromagnetically arranged ($d_2 = d_{\uparrow\downarrow} = d_{\downarrow\uparrow}$). h_1 means there are two electrons in the lower band and one electron in the upper band ($h_1 = h_{1\uparrow} = h_{1\downarrow}$). So under this condition, the interaction term is simplified to

$$\begin{aligned} H_{\text{int}} &= NUs^2 + 2N(U' - J_H)d_1^2 + 2NU'd_2^2 \\ &\quad + 2N(U + 2U' - J_H)h_1^2 \end{aligned} \tag{B13}$$

and the completeness relationship of the slave-bosons Eq. (B5) and the conservation of the number of bosons and electrons [Eq. (B6)] can be expressed as

$$1 = s^2 + 2\left(d_1^2 + d_2^2 + h_1^2\right), \tag{B14}$$

$$n_1 = 2\left(d_1^2 + d_2^2 + h_1^2\right), \tag{B15}$$

$$n_2 = 2\left(s^2 + d_1^2 + d_2^2 + 2h_1^2\right). \tag{B16}$$

With these constraints, the q factor of the hopping term also is simplified:

$$q_1 = \frac{2(1-2d_1^2-2d_2^2-s_1^2)s^2}{(1-s^2)(1+s^2)},$$
$$q_2 = \frac{(1-2d_1^2-2d_2^2-s^2)(d_1+d_2)^2}{2(d_1^2+d_2^2)(1-d_1^2-d_2^2)}. \quad \text{(B17)}$$

We discuss the modification of superconductivity in the next section.

In this work, we only consider paramagnetic solutions, since no long-range magnetic order has been reported in the experiments. The discussion of influence of magnetic solution in the slave-boson calculation is left for future study.

APPENDIX C: BOGOLIUBOV-DE GENNES EQUATION AND SUPERCONDUCTIVITY

We use the BdG method to deal with the superconductivity. First, it should be noticed that there is no coupling between two bands after the slave-boson mean-field approximation. So we can treat the two energy bands respectively as a single band. Thus, the single-band Hamiltonian can be written as:

$$\hat{H}_\alpha = -\sum_{i,\sigma}\mu_\alpha \hat{n}_{i\alpha\sigma} + t_\alpha q_\alpha \sum_{<i,j>,\sigma}(\hat{d}^\dagger_{i\alpha\sigma}\hat{d}_{j\alpha\sigma} + \text{H.c.}) + \frac{1}{4}J_\alpha\sum_{\langle ij\rangle}(4\mathbf{S}_{i\alpha}\cdot\mathbf{S}_{j\alpha} - n_{i\alpha}n_{j\alpha}), \quad \text{(C1)}$$

where $\mu_\alpha = \mu - \epsilon_\alpha$ is the chemical potential of band α. We have ignored the Hund coupling, because the Hund coupling term only depends on slave-boson mean-field parameters. For simplicity, we absorb the coefficient $\frac{1}{4}$ into J_α in the following text, that is, $J_\alpha = \frac{1}{4}J_\alpha$.

Next, by using mean-field approximation and translating it into the k space, we get a new Hamiltonian in the mean-field level [69]:

$$\hat{H}_\alpha = \sum_{k\sigma}[-2(K+t_\alpha)(\cos k_x+\cos k_y) - \mu_\alpha]\hat{d}^\dagger_{k\alpha\sigma}\hat{d}_{k\alpha\sigma} - \sum_k(\Delta_d^*\eta_k\hat{d}_{-k\alpha\downarrow}\hat{d}_{k\alpha\uparrow} + \Delta_d\eta_k\hat{d}^\dagger_{k\alpha\uparrow}\hat{d}^\dagger_{-k\alpha\downarrow}) + \frac{N|\Delta_d|^2}{3J_\alpha} + \frac{4NK^2}{3J_\alpha} + 2J_\alpha N n_\alpha(1-2n_\alpha), \quad \text{(C2)}$$

where $\eta_k = \cos k_x - \cos k_y$, assuming a d-wave symmetry pairing, and we define order parameters as

$$\Delta_d = \frac{3J_\alpha}{N}\sum_k \eta_k\langle\hat{d}_{-k\alpha\downarrow}\hat{d}_{k\alpha\uparrow}\rangle$$
$$K = \frac{3J_\alpha}{2N}\sum_k(\cos k_x+\cos k_y)\langle\hat{d}^\dagger_{k\alpha\sigma}\hat{d}_{k\alpha\sigma}\rangle. \quad \text{(C3)}$$

Before solving the Hamiltonian (C2), we need to consider the influence by slave-bosons. As mentioned in the previous section, slave-boson method modifies hopping term with q factors, so we also introduce the q factors into superconductivity:

$$\hat{H}_\alpha = \sum_{k\sigma}[-2q_\alpha(K+t_\alpha)(\cos k_x+\cos k_y) - \mu_\alpha]\hat{d}^\dagger_{k\alpha\sigma}\hat{d}_{k\alpha\sigma} - q_\alpha\sum_k(\Delta_d^*\eta_k\hat{d}_{-k\alpha\downarrow}\hat{d}_{k\alpha\uparrow} + \Delta_d\eta_k\hat{d}^\dagger_{k\alpha\uparrow}\hat{d}^\dagger_{-k\alpha\downarrow}) + \frac{N|\Delta_d|^2}{3J_\alpha} + \frac{4NK^2}{3J_\alpha} + 2J_\alpha N n_\alpha(1-2n_\alpha). \quad \text{(C4)}$$

And order parameters also be modified by q factors:

$$\Delta_d = \frac{3J_\alpha q_\alpha}{N}\sum_k \eta_k\langle\hat{d}_{-k\alpha\downarrow}\hat{d}_{k\alpha\uparrow}\rangle$$
$$K = \frac{3J_\alpha q_\alpha}{2N}\sum_k(\cos k_x+\cos k_y)\langle\hat{d}^\dagger_{k\alpha\sigma}\hat{d}_{k\alpha\sigma}\rangle. \quad \text{(C5)}$$

So we can conclude that if the electron kinetic energy is zero, then there is no superconductivity in system. To solve the Hamiltonian (C4), we introduce the BdG method. The Bogoliubov transformation of Fermion operator is

$$\hat{d}^\dagger_{k\alpha\uparrow} = \sum_n^{\prime}(u^*_{nk}\hat{\gamma}^\dagger_{nk,\uparrow} + v_{nk}\hat{\gamma}_{n,-k,\downarrow})$$
$$\hat{d}_{-k\alpha\downarrow} = \sum_n^{\prime}(u_{nk}\hat{\gamma}_{n,-k,\downarrow} - v^*_{nk}\hat{\gamma}^\dagger_{nk,\uparrow}), \quad \text{(C6)}$$

where the $'$ over the summation means only sum with positive energy eigenvalue and $\hat{\gamma}^\dagger_{nk\sigma}$ and $\hat{\gamma}_{nk\sigma}$ are the quasiparticle generation and annihilation operators and they satisfy the anticommutation relation. By using Bogoliubov transformation, the diagonalized Hamiltonian can be written as

$$\hat{H}_{\text{eff}} = E_g + \sum_{n,k,\sigma}^{\prime}\hat{\gamma}^\dagger_{nk\sigma}\hat{\gamma}_{nk\sigma}. \quad \text{(C7)}$$

We mark a new kinetic energy parameter as $\varepsilon_k = -2(K + t_\alpha)(\cos k_x + \cos k_y)$ for simplicity. And the commutation relation between the creation (annihilation) operator of electrons and the system Hamiltonian is

$$[\hat{d}^\dagger_{k\alpha\uparrow},\hat{H}_\alpha] = -(q_\alpha\varepsilon_k - \mu_\alpha)\hat{d}^\dagger_{k\alpha\uparrow} + q_\alpha\Delta_d^*\eta_k\hat{d}_{-k\alpha\downarrow},$$
$$[\hat{d}_{-k\alpha\downarrow},\hat{H}_\alpha] = (q_\alpha\varepsilon_k - \mu_\alpha)\hat{d}_{-k\alpha\downarrow} + q_\alpha\Delta_d^*\eta_k\hat{d}^\dagger_{k\alpha\uparrow}. \quad \text{(C8)}$$

Substitute Eq. (C6) and Eq. (C7) into Eq. (C8) and compare the coefficients of the quasiparticle operators on both sides of the equation. We can get the coupled equations of coefficients $\{u_{nk}, v_{nk}\}$:

$$E_{nk}\begin{pmatrix}u_{nk}\\ v_{nk}\end{pmatrix} = \begin{pmatrix}q_\alpha\varepsilon_k - \mu_\alpha & q_\alpha\Delta_d\eta_k\\ q_\alpha\Delta_d^*\eta_k & -q_\alpha\varepsilon_k + \mu_\alpha\end{pmatrix}\begin{pmatrix}u_{nk}\\ v_{nk}\end{pmatrix}. \quad \text{(C9)}$$

The self-consistent equations of mean-field order parameter and number of density can be written as

$$\Delta_d = -\frac{3J_\alpha q_\alpha}{N}\sum_{nk}\eta_k u_{nk}v^*_{nk}n_F(E_{nk}),$$
$$K = \frac{3J_\alpha q_\alpha}{2N}\sum_{nk}(\cos k_x+\cos k_y)|u_{nk}|^2 n_F(E_{nk}),$$
$$n_\alpha = \frac{2}{N}\sum_{nk}|u_{nk}|^2 n_F(E_{nk}), \quad \text{(C10)}$$

where $n_F(E_{nk})$ is the Fermi-Dirac distribution with energy E_{nk}. Using the self-consistent iteration of Eq. (C9) and Eq. (C10), we can get the mean-field order parameters. The last point to mention is that although the superconducting order parameter Δ_d is written here as a complex number, it is actually a real number under the conditions we consider.

APPENDIX D: DISCUSSION ON R 5*d* ELECTRONS

In the main text, we only keep two correlated Ni 3*d* orbitals in the construction of effective model by neglecting the 5*d* electron band from the rare-earth element. Here we present several remarks and explain why we discard the R 5*d* electron band in the effective model.

(1) We notice that, in a recent experiment on the $Nd_6Ni_5O_{12}$ compound [74,75] (which hosts a $3d^{8.8}$ configuration, named $n = 5$ in series $R_{n+1}Ni_nO_{2n+1}$), superconductivity survives and shows very similar behavior with infinite nickelates ($n = \infty$). However, the 5*d* band around the Fermi level of the $Nd_6Ni_5O_8$ compound is totally different from that in infinite nickelates: Instead of a $5d_{z^2}$ band around the Γ point, $Nd_6Ni_5O_8$ shows a $5d_{xy}$ band around the M point. This dramatic 5*d* band difference, but with the similar superconducting behavior, strongly supports that the 5*d* band from rare earth is irrelevant to superconductivity.

(2) In infinite-layer nickelates, the band around the Γ point is mainly made of the $5d_{z^2}$ orbital, which has sizable hybridization with the Ni $3d_{z^2}$ orbital. However, as we elucidated in the main text, both RIXS experiment [52] and our calculations show that the Ni $3d_{z^2}$ orbital is deeply below the Fermi level and hardly contributes to the physics in the NiO_2 plane. Thus, if we focus on the nature of superconductivity, that is believed to occur in the NiO_2 plane, then it is reasonable to neglect the 5*d* band around the Γ point in the effective model.

(3) In infinite-layer nickelates, under hole-doping, the 5*d* band around the Γ point quickly vanishes (or its contribution around the Fermi level vanishes), which implies this 5*d* band is irrelevant to the superconducting nature [34].

Based on the above reasons, we speculate that the 5*d* band from rare-earth elements contributes to modifying the electron correlations on the Ni $3d_{z^2}$ orbital through the hybridization effect and to serving as a charge reservoir. In this regard, the existence of an R 5*d* band can explain that the charge carriers changes from electron-like to holelike on hole doping in the Hall measurement. That is, the existence of an R 5*d* band contributes to electron-like carriers in the parent compound, and then these electron-like carriers continue reduce on hole doping. At the critical doping level, the contribution of the R 5*d* band around the Fermi level vanishes, so that the carrier type becomes holelike. This is confirmed in many DFT calculations, e.g., Ref. [34].

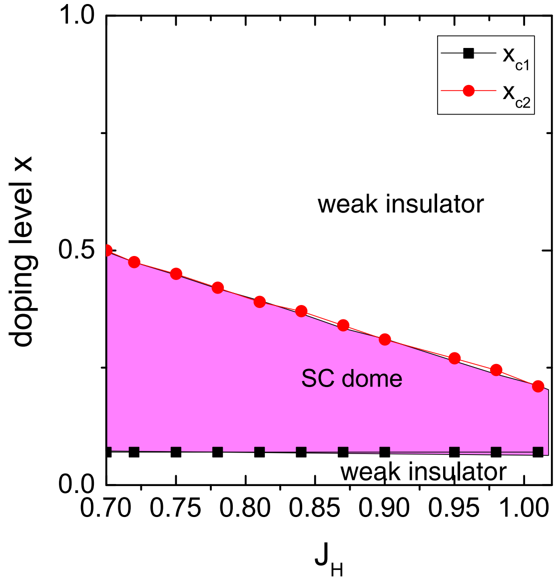

FIG. 12. Critical doping level of superconducting dome as a function of Hund's coupling J_H.

Last, we also notice that RIXS data cannot fully exclude the contributions of Nd 5*d* orbitals when doing atomic multiple calculations [52]. The detailed role of Nd 5*d* orbitals needs a careful study in the future.

APPENDIX E: SUPERCONDUCTING CRITICAL DOPING LEVEL

In the main text, we discuss the superconducting dome and related critical doping level at a given Hund exchange strength $J_H = 0.7$ eV. In this section, we discuss how the superconducting dome evolves as a function of J_H. Figure 12 shows the dependence of critical doping levels as a function of Hund's interaction J_H (by fixing other parameters). $X_{c1}(X_{c2})$ is the lower (upper) critical doping level and the superconducting dome appears within $X_{c1} < x < X_{c2}$. As we see, the lower critical doping level X_{c1} is independent of J_H while the upper critical doping level X_{c2} is gradually suppressed with increased J_H. Thus by choosing $J_H \sim 0.85$ eV, the obtained critical doping level is comparable with experiments. Such a Hund's coupling is actually a large value and the commonly used J_H for nickel is about 0.7 eV in DFT+DMFT calculation, so we use 0.7 eV in the paper for illustration.

[1] J. G. Bednorz and K. A. Müller, Z. Phys. B **64**, 189 (1986).
[2] B. Keimer, S. A. Kivelson, M. R. Norman, S. Uchida, and J. Zaanen, Nature (Lond.) **518**, 179 (2015).
[3] F. C. Zhang and T. M. Rice, Phys. Rev. B **37**, 3759 (1988)
[4] P. A. Lee, N. Nagaosa, and X.-G. Wen, Rev. Mod. Phys. **78**, 17 (2006).
[5] J. Zaanen, G. A. Sawatzky, and J. W. Allen, Phys. Rev. Lett. **55**, 418 (1985).
[6] Y. Kamohara, T. Watanabe, M. Hirano, and H. Hosono, J. Am. Chem. Soc. **130**, 3296 (2008).
[7] G. R. Stewart, Rev. Mod. Phys. **83**, 1589 (2011).
[8] Q. Si, R. Yu, and E. Abrahams, Nat. Rev. Mater. **1**, 16017 (2016).
[9] A. Chubukov, Annu. Rev. Condens. Matter Phys. **3**, 57 (2012).
[10] A. Georges, L. de'Medici, and J. Mravlje, Annu. Rev. Condens. Matter Phys. **4**, 137 (2013).

[11] D. Li, K. Lee, B. Y. Wang, M. Osada, S. Crossley, H. R. Lee, Y. Cui, Y. Hikita, and H. Y. Hwang, Nature (Lond.) **572**, 624 (2019).

[12] S. Zeng, C. S. Tang, X. Yin, C. Li, M. Li, Z. Huang, J. Hu, W. Liu, G. J. Omar, H. Jani, Z. S. Lim, K. Han, D. Wan, P. Yang, S. J. Pennycook, A. T. S. Wee, and A. Ariando, Phys. Rev. Lett. **125**, 147003 (2020).

[13] D. Li, B. Wang, K. Lee, Shannon P. Harvey, M. Osada, B. H. Goodge, L. F. Kourkoutis, and H. Y. Hwang, Phys. Rev. Lett. **125**, 027001 (2020).

[14] M. Osada, B. Y. Wang, B. H. Goodge, S. P. Harvey, K. Lee, D. Li, L. F. Kourkoutis, and H. Y. Hwang, Adv. Mater. **33**, 2104083 (2021).

[15] S. W. Zeng, C. J. Li, L. E. Chow, Y. Cao, Z. T. Zhang, C. S. Tang, X. M. Yin, Z. S. Lim, J. X. Hu, P. Yang, and A. Ariando, Sci. Adv. **8**, eabl9927 (2022).

[16] M. Osada, B. Y. Wang, K. Lee, D. Li, and H. Y. Hwang, Phys. Rev. Mater. **4**, 121801(R) (2020).

[17] Q. Gu, Y. Li, S. Wan, H. Li, W. Guo, H. Yang, Q. Li, X. Zhu, X. Pan, Y. Nie, and H.-H. Wen, Nat. Commun. **11**, 6027 (2020).

[18] M. Osada, B. Y. Wang, B. H. Goodge, K. Lee, H. Yoon, K. Sakuma, D. Li, M. Miura, L. F. Kourkoutis, and H. Y. Hwang, Nano Lett. **20**, 5735 (2020).

[19] N. N. Wang, M. W. Yang, K. Y. Chen, Z. Yang, H. Zhang, Z. H. Zhu, Y. Uwatoko, X. L. Dong, K. J. Jin, J. P. Sun, and J.-G. Cheng, arXiv:2109.12811.

[20] A. S. Botana and M. R. Norman, Phys. Rev. X **10**, 011024 (2020).

[21] H. Sakakibara, H. Usui, K. Suzuki, T. Kotani, H. Aoki, and K. Kuroki, Phys. Rev. Lett. **125**, 077003 (2020).

[22] Y. Nomura, M. Hirayama, T. Tadano, Y. Yoshimoto, K. Nakamura, and R. Arita, Phys. Rev. B **100**, 205138 (2019).

[23] Z. Liu, Z. Ren, W. Zhu, Z. F. Wang, and J. Yang, npj Quantum Mater. **5**, 31 (2020).

[24] M. Jiang, M. Berciu, and G. A. Sawatzky, Phys. Rev. Lett. **124**, 207004 (2020).

[25] X. Wu, D. DiSante, T. Schwemmer, W. Hanke, H. Y. Hwang, S. Raghu, and R. Thomale, Phys. Rev. B **101**, 060504(R) (2020).

[26] M. Kitatani, L. Si, O. Janson, R. Arita, Z. Zhong, and K. Held, npj Quantum Mater. **5**, 59 (2020).

[27] G.-M. Zhang, Y.-F. Yang, and F.-C. Zhang, Phys. Rev. B **101**, 020501(R) (2020).

[28] Z. Wang, G.-M. Zhang, Y.-F. Yang, and F.-C. Zhang, Phys. Rev. B **102**, 220501(R) (2020).

[29] E. Been, W.-S. Lee, H. Y. Hwang, Y. Cui, J. Zaanen, T. Devereaux, B. Moritz, and C. Jia, Phys. Rev. X **11**, 011050 (2021)

[30] H. Lu, M. Rossi, A. Nag, M. Osada, D. F. Li, K. Lee, B. Y. Wang, M. Garcia-Fernandez, S. Agrestini, Z. X. Shen, E. M. Been, B. Moritz, T. P. Devereaux, J. Zaanen, H. Y. Hwang, K.-J. Zhou, and W. S. Lee, Science **373**, 213 (2021).

[31] P. Adhikary, S. Bandyopadhyay, T. Das, I. Dasgupta, and T. Saha-Dasgupta, Phys. Rev. B **102**, 100501(R) (2020).

[32] E. M. Nica and O. Erten, Phys. Rev. B **102**, 214509 (2020).

[33] C. Peng, H.-C. Jiang, B. Moritz, T. P. Devereaux, and C. Jia, arXiv:2110.07593.

[34] Z. Liu, C. Xu, C. Cao, W. Zhu, Z. F. Wang, and J. Yang, Phys. Rev. B **103**, 045103 (2021).

[35] J. Gao, Z. Wang, C. Fang, and H. Weng, Natl. Sci. Rev. **8**, nwaa218 (2021).

[36] E. M. Nica, J. Krishna, R. Yu, Q. Si, A. S. Botana, and O. Erten, Phys. Rev. B **102**, 020504(R) (2020).

[37] J. Karp, A. Hampel, M. Zingl, A. S. Botana, H. Park, M. R. Norman, and A. J. Millis, Phys. Rev. B **102**, 245130 (2020).

[38] H. LaBollita and A. S. Botana, Phys. Rev. B **104**, 035148 (2021).

[39] Y. Gu, S. Zhu, X. Wang, J. Hu, and H. Chen, Commun. Phys. **3**, 84 (2020).

[40] L.-H. Hu and C. Wu, Phys. Rev. Res. **1**, 032046(R) (2019).

[41] P. Werner and S. Hoshino, Phys. Rev. B **101**, 041104(R) (2020).

[42] F. Lechermann, Phys. Rev. B **101**, 081110(R) (2020).

[43] F. Lechermann, Phys. Rev. X **10**, 041002 (2020).

[44] Y. Wang, C.-J. Kang, H. Miao, and G. Kotliar, Phys. Rev. B **102**, 161118(R) (2020).

[45] B. Kang, C. Melnick, P. Semon, G. Kotliar, and S. Choi, arXiv:2007.14610.

[46] C.-J. Kang and G. Kotliar, Phys. Rev. Lett. **126**, 127401 (2021).

[47] X. Wan, V. Ivanov, G. Resta, I. Leonov, and S. Y. Savrasov, Phys. Rev. B **103**, 075123 (2021).

[48] S. Ryee, M.-J. Han, and S. Choi, Phys. Rev. Lett. **126**, 206401 (2021).

[49] T. Plienbumrung, M. Daghofer, and A. M. Oles, Phys. Rev. B **103**, 104513 (2021).

[50] F. Petocchi, V. Christiansson, F. Nilsson, F. Aryasetiawan, and P. Werner, Phys. Rev. X **10**, 041047 (2020).

[51] C. Lu, L. H. Hu, Y. Wang, F. Yang, and C. Wu, Phys. Rev. B **105**, 054516 (2022).

[52] M. Rossi, H. Lu, A. Nag, D. Li, M. Osada, K. Lee, B. Y. Wang, S. Agrestini, M. Garcia-Fernandez, J. J. Kas, Y.-D. Chuang, Z. X. Shen, H. Y. Hwang, B. Moritz, K.-J. Zhou, T. P. Devereaux and W. S. Lee, Phys. Rev. B **104**, L220505 (2021).

[53] P. Jiang, L. Si, Z. Liao, and Z. Zhong, Phys. Rev. B **100**, 201106(R) (2019).

[54] I. Leonov, S. L. Skornyakov, and S. Y. Savrasov, Phys. Rev. B **101**, 241108(R) (2020).

[55] J. Karp, A. S. Botana, M. R. Norman, H. Park, M. Zingl, and A. Millis, Phys. Rev. X **10**, 021061 (2020).

[56] H. Zhang, L. Jin, S. Wang, B. Xi, X. Shi, F. Ye, and J.-W. Mei, Phys. Rev. Res. **2**, 013214 (2020).

[57] V. Olevano, F. Bernardini, X. Blase, and A. Cano, Phys. Rev. B **101**, 161102(R) (2020).

[58] Y.-H. Zhang and A. Vishwanath, Phys. Rev. Res. **2**, 023112 (2020).

[59] S. Leontica, C. Lee, B. Singh, J. Nokelainen, B. Barbiellini, R. S. Markiewicz, A. Bansil, and J. Sun, Commun. Phys. **4**, 112 (2021).

[60] M. Hepting D. Li, C. J. Jia, H. Lu, E. Paris, Y. Tseng, X. Feng, M. Osada, E. Been, Y. Hikita, Y.-D. Chuang, Z. Hussain, K. J. Zhou, A. Nag, M. Garcia-Fernandez, M. Rossi, H. Y. Huang, D. J. Huang, Z. X. Shen, T. Schmitt, H. Y. Hwang *et al.*, Nat. Mater. **19**, 381 (2020).

[61] B. H. Goodge, D. Li, K. Lee, M. Osada, B. Y. Wang, G. A. Sawatzky, H. Y. Hwang, and L. F. Kourkoutis, Proc. Natl. Acad. Sci. USA **118**, e2007683118 (2021).

[62] Y. Shen, J. Sears, G. Fabbris, J. Li, J. Pelliciari, I. Jarrige, Xi He, I. Bozovic, M. Mitrano, Junjie Zhang, J. F. Mitchell, A. S. Botana, V. Bisogni, M. R. Norman, S. Johnston, and M. P. M. Dean, Phys. Rev. X **12**, 011055 (2022).

[63] V. M. Katukuri, N. A. Bogdanov, O. Weser, J. van den Brink, and A. Alavi, Phys. Rev. B **102**, 241112(R) (2020).

[64] F. Aryasetiawan, M. Imada, A. Georges, G. Kotliar, S. Biermann, and A. I. Lichtenstein, Phys. Rev. B **70**, 195104 (2004).

[65] T. Miyake and F. Aryasetiawan, Phys. Rev. B **77**, 085122 (2008).

[66] L. Vaugier, H. Jiang, and S. Biermann, Phys. Rev. B **86**, 165105 (2012).

[67] A. van Roekeghem, L. Vaugier, H. Jiang, and S. Biermann, Phys. Rev. B **94**, 125147 (2016).

[68] G. Kotliar and A. E. Ruckenstein, Phys. Rev. Lett. **57**, 1362 (1986).

[69] G. Kotliar and J. Liu, Phys. Rev. B **38**, 5142 (1988).

[70] A. Rüegg, M. Indergand, S. Pilgram, and M. Sigrist, Eur. Phys. J. B **48**, 55 (2005).

[71] X. Zhou, X. Zhang, J. Yi, P. Qin, Z. Feng, P. Jiang, Z. Zhong, H. Yan, X. Wang, H. Chen, H. Wu, X. Zhang, Z. Meng, X. Yu, M. B. H. Breese, J. Cao, J. Wang, C. Jiang, and Z. Liu, Adv. Mater. **34**, 2106117 (2022).

[72] J. Q. Lin, P. Villar Arribi, G. Fabbris, A. S. Botana, D. Meyers, H. Miao, Y. Shen, D. G. Mazzone, J. Feng, S. G. Chiuzbăian, A. Nag, A. C. Walters, M. García-Fernández, K.-J. Zhou, J. Pelliciari, I. Jarrige, J. W. Freeland, J. Zhang, J. F. Mitchell, V. Bisogni, X. Liu *et al.*, Phys. Rev. Lett. **126**, 087001 (2021).

[73] R. A. Ortiz, P. Puphal, M. Klett, F. Hotz, R. K. Kremer, H. Trepka, M. Hemmida, H.-A. Krug von Nidda, M. Isobe, R. Khasanov, H. Luetkens, P. Hansmann, B. Keimer, T. Schäfer, and M. Hepting, Phys. Rev. Research **4**, 023093 (2022).

[74] G. A. Pan, D. F. Segedin, H. LaBollita, Q. Song, E. M. Nica, B. H. Goodge, A. T. Pierce, S. Doyle, S. Novakov, D. Córdova Carrizales, A. T. N'Diaye, P. Shafer, H. Paik, J. T. Heron, J. A. Mason, A. Yacoby, L. F. Kourkoutis, O. Erten, C. M. Brooks, A. S. Botana, and J. A. Mundy, Nat. Mater. **21**, 160 (2022).

[75] H. LaBollita and A. S. Botana, Phys. Rev. B **105**, 085118 (2022).

[76] M. P. Teter, M. C. Payne, and D. C. Allan, Phys. Rev. B **40**, 12255 (1989).

[77] G. Kresse and J. Furthmüller, Phys. Rev. B **54**, 11169 (1996).

[78] P. E. Blöchl, Phys. Rev. B **50**, 17953 (1994).

[79] J. P. Perdew, K. Burke, and M. Ernzerhof, Phys. Rev. Lett. **77**, 3865 (1996).

[80] A. A. Mostofi, J. R. Yates, Y.-S. Lee, I. Souza, D. Vanderbilt, and N. Marzari, Comput. Phys. Commun. **178**, 685 (2008).

[81] H. Eskes, L. H. Tjeng, and G. A. Sawatzky, Phys. Rev. B **41**, 288 (1990).

[82] T. Siegrist, S. M. Zahurak, D. W. Murphy, and R. S. Roth, Nature (Lond.) **334**, 231 (1988).

[83] L. Hozoi, L. Siurakshina, P. Fulde, and J. van den Brink, Sci. Rep. **1**, 65 (2011).

[84] M Moretti Sala, V. Bisogni, C. Aruta, G. Balestrino, H. Berger, N. B. Brookes, G. M. de Luca, D. D. Castro, M. Grioni, M. Guarise, P. G. Medaglia, F. M. Granozio, M. Minola, P. Perna, M. Radovic, M. Salluzzo, T. Schmitt, K. J. Zhou, L. Braicovich, and G. Ghiringhelli, New J. Phys. **13**, 043026 (2011).

[85] C. Jayaprakash, H. R. Krishnamurthy, and S. Sarker, Phys. Rev. B **40**, 2610 (1989).

[86] P. Coleman, Phys. Rev. B **29**, 3035 (1984).